Supplementary Information (SI) for Energy & Environmental Science.
This journal is © The Royal Society of Chemistry 2025

Electronic Supplementary Information

Nanofluidic-enhanced high-mass-loading electrodes for energy-dense and high-rate lithium-sulfur batteries

Chunlei Song,[a] Lyuming Pan,[a] Lu Chen,[a] Yanxin Jiang,[a] Hongji Pan, [a] He Zhao, [a] Nanshan Chen, [a] Zhiqiang Yang, [a] Liu Yang, [a] Qing Yan, [a,d] Xudong Peng,[*c] Xiaohua Ma,[a,e] Yiju Li,[*a,b] and Tianshou Zhao[*a,b]

[a] Department of Mechanical and Energy Engineering, Southern University of Science and Technology, Shenzhen, 518055, P.R. China

[b] SUSTech Energy Institute for Carbon Neutrality, Southern University of Science and Technology, Shenzhen, 518055, P.R. China

[c] School of Advanced Engineering, Great Bay University, Dongguan, Guangdong, 523000, P.R. China

[d] School of Biological and Chemical Engineering, NingboTech University, Ningbo, 315100, P.R. China

[e] School of Chemistry and Chemical Engineering, North Minzu University, Yinchuan, 750021, P.R. China

[*]Corresponding authors: xpengal@connect.ust.hk (Xudong Peng); liyj6@sustech.edu.cn (Yiju Li); zhaots@sustech.edu.cn (Tianshou Zhao)

1. Experimental Details

1.1 Chemicals

Multiwalled carbon nanotubes (CNTs, >99.0%) were purchased from Nanjing Xianfeng Nano Co. Ltd (Jiangsu, China). Sulfur was purchased from Shanghai Adamas-beta Reagent Co., 1,3,5-triformylbenzene, 1,4-diaminobenzene, 1,4-dioxane, pyruvic acid, acetone, tetrahydrofuran (THF) and glacial acetic acid were purchased from TENSUS BIOTECH (shanghai, China). All chemicals were analytical grade and used without further purification. The copper foil, aluminum foil, Carbon black (Super-P), Celgard 2500, 2032-type coin-cell cases, springs, and spacers and metallic Li foil (thickness: 50 µm, 450 um, Li content ≥99.9%) were obtained from Canrd Technology Co. Ltd.

1.2 Synthesis of 4-carboxyl-quinoline linked covalent organic frameworks

A 10 mL Schlenk tube was filled with 1,3,5-triformylbenzene (48.0 mg, 0.30 mmol), 1,4-diaminobenzene (48.0 mg, 0.45 mmol), glacial acetic acid (100.0 µL) and 1,4-dioxane (3.0 mL). The tube was first sonicated for 10 min, then pyruvic acid (62.5 µL, 0.9 mmol) was added with vortex. Subsequently, the tube was charged with a degassing-filling cycle using a Schlenk line under 77 K in a liquid N_2 bath and sealed. The reaction was heated at 120 ˚C for 72 h yielding a precipitate that was isolated by suction filtration, washed with acetone (30.0 mL) and THF (30.0 mL) three times, and dried in a vacuum oven at 60 ˚C for 10 h.

1.3 Fabrication of IGCL-NFE membranes for nanofluidic devices

For the preparation of the IGCL-NFE membrane, 80.0 mg 4-carboxyl-quinoline linked covalent organic frameworks, 10.0 mg polyvinylidene difluoride (PVDF) was dissolved into N-methyl-2-pyrrolidone (NMP) solvent to generate a homogenous solution. The mixture was then vigorously stirred for 12 h at room temperature. The prepared dispersion was then coated onto an aluminum foil using a spread coating method and dried under 100 ˚C to obtain the IGCL-NFE membrane.

1.4 Preparation of S, S/IGCL-NFE and S/IGCL-NFE dry cathodes

Impregnation of sulfur was carried out by a melt-diffusion method. Briefly, 80 wt% CNT/sulfur composite powder was transferred into a high-temperature reaction vessel and heated at 155 °C for 10 h, resulting in the 80 wt% CNT/sulfur composite. CNT/sulfur/IGCL-NFE (in a 10:40:2 weight ratio) was prepared by the same method under similar conditions. For the wet cathodes of S and S/IGCL-NFE, sulfur cathodes were achieved by a slurry casting method. 80 wt% CNT/sulfur

composite or CNT/sulfur/IGCL-NFE (in a 10:40:2 weight ratio) powder, 10 wt% Super-P, and 10 wt% LA132 binder were mixed in n-propyl alcohol to form a slurry then coated on aluminum current collectors and dried at 55 ˚C in a vacuum oven for 12 h. For the S/IGCL-NFE dry cathodes, firstly, mix the prepared S/IGCL-NFE composite cathode (95 wt%), Super-P (3 wt%), and PTFE (2 wt%) (DuPont, USA). After manually grinding the mixture for 10 minutes, a uniform thick sheet will be formed. Finally, the thick sheet is placed on a roller pressing machine heated to 50 °C and rolled to the desired thickness. All operations are conducted in an argon-filled glove box.

1.5 Materials characterizations

The X-ray powder diffraction patterns of the covalent organic frameworks were tested on a Bruker D8 Advance diffractometer with a Cu target tube and a graphite monochromator (40 kV and 40 mA). A scanning electron microscope (SEM) (ZEISS Merlin) was used to acquire the morphologies of anodes and cathodes. The spectroscopic characteristics of the covalent organic frameworks were revealed with Fourier transform infrared spectroscopy (FTIR, Thermo Scientific NICOLET IS50). The sulfur weight content of all samples was measured by thermogravimetric analysis using a simultaneous thermal analyzer (Rigaku) with a heating rate of 5 ˚C min^{-1} from room temperature to 500 ˚C under N_2 flow. Scanning electrochemical microscopy (SECM) tests were performed on the CHI920D Electrochemical workstation (Chenhua, Shanghai). The Zeta potential at room temperature was determined using the Malvern Zetasizer Nano ZS90 testing machine. The Raman spectra were obtained by HORIBA LabRAM HR Evolution with a laser wavelength of 785 nm and wavenumber from 600-900 cm^{-1}. The time-of-flight secondary ion mass spectroscopy (TOF-SIMS) tests with high ion detection sensitivity were carried out by TOF-SIMS (ION-TOF GmbH), with a sputtering time of 800 s, within an area of 300 μm*300 μm.

1.6 Electrochemical measurements

CR2032 coin cells were employed and assembled in an argon-filled glove box using the as-prepared S cathode or S/IGCL-NFE cathode, separator, and Li metal anode. The electrolyte for battery tests is 1 M Lithium bis(trifluoromethanesulfonyl)imide (LiTFSI) in DOL/DME=1/1 vol with 2 wt% $LiNO_3$ addition. A commercial Celgard 2500 was used as the separator. For the cell with sulfur loading of 1.0 mg cm^{-2}, the E/S usage ratio is controlled at around 9.0 μL mg^{-1} and N/P is 5.4 for a typical electrode. For the cells with sulfur loading of 2.0, 4.0 and 4.1 mg cm^{-2}, the E/S usage ratio is controlled at around 5.0 μL mg^{-1} and N/P is ~3.0 for a typical electrode. For the coin cells with

larger sulfur loading (>5.0 mg cm^{-2}), 30 μL electrolyte was injected into each cell and N/P is 3.0 for a typical electrode. For the pouch cells, the E/S usage ratio is controlled at around 3.0 μL mg^{-1} and N/P is 1.27. The galvanostatic intermittent titration technique (GITT) was operated using the LANHE Battery Testing System (Wuhan, China). The electrochemical impedance spectroscopy (EIS) was tested by CHI760e (Shanghai, China). Galvanostatic discharge/charge curves, rate, and cycling performance of Li-S cells were tested by a LAND CT2001A instrument with a voltage window between 1.6-2.8 V. The tested drone weighs 82.1 g.

Scanning electrochemical microscope (SECM) tests were performed on the CHI920D Electrochemical workstation (Chenhua, Shanghai, China). The CHI116 microprobe and Al electrodes were used as the first and second working electrodes, Li foil was used as the reference electrode, and the platinum wire electrode was assembled into a four-electrode system. The working solution is 10 mM 2,5-ditertbutyl-1,4-dimethoxybenzene (DBDMB) + 1 M LiTFSI in DOL/DME=1/1 vol, in which DBDMB was used as the redox medium.

For the pressure study, the M1616S sensor (Crownto, China) was used for pressure sensing with a maximum sensing area of 5.5 × 5.5 cm^2, minimum pressure sensing range of >10 g cm^{-2}, and the 2D pressure sensor has 256 nodes for an area of 4.0 × 4.0 cm^2, and thus, the areal sensing resolution is 0.0625 cm^2. The sensor with a maximum sensing speed of 30 Hz and M1616S software was used for pressure calibration and mapping analysis. The pressure distribution map of the Li-S pouch cell is based on 25 nodes in the central area. The area of pouch battery:16.0 cm^2. Pressure values were recorded at intervals of 1 s for 0.05 C rate at a sulfur loading of 8.0 mg cm^{-2}. For the Li//S pouch cell (single layer) (cathode area: 4.0 × 4.0 cm^2), The Li foil (area: 4.0 × 4.0 cm^2) with an areal capacity of 10.0 mAh cm^{-2} and Celgard 2500 (area: 4.0 × 4.0 cm^2) were used as the anode and separator, respectively.

The effective electronic conductivities of S and S/IGCL-NFE were measured using an ion-blocking symmetric cell configuration. 100.0 mg of powders were loaded within a PEEK cylinder with an inner diameter of 10 mm and cold-pressed at a pressure of 300 MPa for 1 min. The thickness of the pellet was measured as 0.644 mm for S, and 0.745 mm for S/IGCL-NFE with a spiral micrometer after measurement. After resting for 1 h under open circuit conditions, the applied potentials were applied in the following sequence: -20, -10, -5, -2, +2, +5, +10, and +20 mV, each maintained for an equilibration period of 20 mins.

The effective ionic conductivities of S and S/IGCL-NFE were measured using an electron-blocking symmetric cell configuration. First, 100.0 mg of powders were loaded within a PEEK with an inner diameter of 10 mm and cold-pressed at a pressure of 300 MPa for 1 min. Next, 100 mg LPSC powder was loaded into the working and counter electrode compartments and cold-pressed at a pressure of 300 MPa for 1 min. Finally, a Li-In alloy was sequentially placed in the working and counter electrode side and cold-pressed for 1 min under a pressure of 200 MPa. After resting for 12 h under open circuit conditions, the sequence of the applied potentials consisted of the following steps: -40, -30, -20, +20, +30, and +40 mV, each maintained for an equilibration period of 20 mins.

The total electronic and ionic resistance of the composite cathode can be calculated using Ohm's Law (R_k, where k = e^- or Li^+). By integrating the current response under varied voltages, the geometric area (A = 0.785 cm^2), and the thickness of the electrode, the effective ionic/electronic conductivity (σ_k) within the composite cathode can be calculated using Equation:

$$\sigma_k = \frac{d}{AR_k}$$

2 Multi-physical coupling Simulations

The electrochemical behavior of the Li-S battery was modeled using the finite element method implemented in COMSOL Multiphysics 6.2. The model incorporates the Nernst-Planck equations for mass and charge transport, Butler-Volmer kinetics for charge transfer, and thermodynamic equations to describe open-circuit potentials. Precipitation and dissolution reactions of solid sulfur (S_8) and lithium sulfide (Li_2S) were also included to account for phase changes during operation.

2.1 Electrochemical Reactions

Electrochemical reactions were modeled at the cathode-electrolyte interface. At the interface of the electrolyte and the anode, the reaction process of Li-ions can be described by the simplified reaction:

$$Li^+ + e^- \rightleftharpoons Li \qquad (1)$$

The reduction of solid sulfur (S_8(s)) into polysulfides and eventually into lithium sulfide follows a sequence of reactions:

$$\frac{1}{2}S_8 + e^- \rightleftharpoons \frac{1}{2}S_8^{2-} \quad (2)$$

$$\frac{3}{2}S_8^{2-} + e^- \rightleftharpoons 2S_6^{2-} \quad (3)$$

$$S_6^{2-} + e^- \rightleftharpoons \frac{3}{2}S_4^{2-} \quad (4)$$

$$\frac{1}{2}S_4^{-2} + e^- \rightleftharpoons S_2^{2-} \quad (5)$$

$$\frac{1}{2}S_2^{2-} + e^- \rightleftharpoons S^{2-} \quad (6)$$

Charge transfer at the electrode-electrolyte interfaces was modeled using the Butler-Volmer equation to describe reaction kinetics:

$$i = i_{ex,j}\left[\prod_i \left(\frac{C_i}{C_{i,ref}}\right)^{p_{i,j}} exp\left(\frac{\alpha_{a,j}F\eta_j}{RT}\right) - \prod_i \left(\frac{C_i}{C_{i,ref}}\right)^{q_{i,j}} exp\left(\frac{\alpha_{c,j}F\eta_j}{RT}\right)\right] \quad (7)$$

where $i_{ex,j}$ is the exchange current density, $\alpha_{a,j}$ and $\alpha_{c,j}$ are the anodic and cathodic transfer coefficients, C_i and $C_{i,ref}$ are the local and reference species concentrations, and η_j is the reaction overpotential given by:

$$\eta_j = \phi_s - \phi_e - U_{eq} \quad (8)$$

where ϕ_s and ϕ_e are the solid phase and electrolyte potentials, respectively, and U_{eq} is the equilibrium potential.

2.2 Mass and Charge Transport

Mass transport in the liquid electrolyte was modeled by the Nernst-Planck equation, which captures ion migration due to the electric field and diffusion driven by concentration gradients:

$$N_{i,m} = -D_{i,m}\left(\nabla C_{i,m} + \frac{z_i F}{RT} C_{i,m}\nabla\phi\right) \quad (9)$$

where $D_{i,m}$ is the diffusion coefficient of species i, $C_{i,m}$ is the species concentration, z_i is the charge number, F is Faraday's constant, R is the universal gas constant, T is the temperature, and ϕ is the electrolyte potential. The species considered include Li^+, polysulfide ions (S_8^{2-}, S_6^{2-}, S_4^{2-}, S_2^{2-}, S^{2-}), and $TFSI^-$, the anion of the lithium salt.

2.3 Precipitation and Dissolution Reactions

Non-faradaic precipitation and dissolution reactions of S_8 and Li_2S were included:

$$S_8(s) \rightleftharpoons S_8(l) \quad (10)$$

$$2Li^+ + S^{2-} \rightleftharpoons Li_2S(s) \quad (11)$$

The rates of these reactions were governed by kinetic parameters, solubility limits, and the

concentrations of reactant species. The precipitation and dissolution of solid sulfur (S_8) and lithium sulfide (Li_2S) were modeled as kinetically controlled processes:

$$R_k = K_k\left(\prod_i C_i^{v_{i,k}} - K_{sp,k}\right) \tag{12}$$

where R_k is the reaction rate, K_k is the rate constant, $K_{sp,k}$ is the solubility product, and $v_{i,k}$ is the stoichiometric coefficient of ionic species i in solid species k.

2.4 Mechanical Behavior

The mechanical behavior of the battery during discharge was analyzed using Hooke's Law for linear elasticity:

$$\sigma_{i,j} = \frac{E}{1+\nu}(\nabla u + (\nabla u)^T) + \frac{2\nu E}{1-2\nu}Tr(\nabla u)\delta_{i,j} \tag{13}$$

where $\sigma_{i,j}$ is the stress tensor, E is Young's modulus, ν is Poisson's ratio, and u is the displacement vector. The displacement of the cathode surface due to the precipitation of Li_2S was calculated as:

$$u_n = \frac{AR}{M\rho} \tag{14}$$

Where A is the cathode surface area, R is the precipitation rate, M and ρ are the molar mass and density of Li_2S.

2.5 Simulation Parameters

The model was simulated at discharge rates of 2 and 5 C under 25 ℃ and 1 C under -20 ℃. Fixed boundary conditions were applied to the battery ends, with roller constraints on other surfaces. Cathode particles had a radius of 1 μm, and the length of nanofluidic channels is 0.1 μm and the pore size is 1.4 nm. The cathode utilization was defined as the volume fraction of Li_2S generated compared to the theoretical maximum. Relevant parameters, including material properties and reaction kinetics, were adapted from previous reports[1] to ensure the reliability of the model.

Table of Contents

Fig. S22. Polysulfides distributions for the Li_2S-forming reaction in the bare S and S/IGCL-NFE models with a current density of 2 C at 25 ˚C.
Fig. S23. Polysulfides distributions for the Li_2S-forming reaction in the bare S and S/IGCL-NFE models with a current density of 5 C at 25 ˚C.
Fig. S24. Polysulfides distributions for the Li_2S-forming reaction in the bare S and S/IGCL-NFE models with a current density of 1 C at -20 ˚C.
Fig. S25. Simulated electrode expansion stress after S_8 was converted into Li_2S in the bare S and S/IGCL-NFE models with a current density of 2 C at 25 ˚C.
Fig. S26. Simulated electrode expansion stress after S_8 was converted into Li_2S in the bare S and S/IGCL-NFE models with a current density of 5 C at 25 ˚C.
Fig. S27. Simulated electrode expansion stress after S_8 was converted into Li_2S in the bare S and S/IGCL-NFE models with a current density of 1 C at -20 ˚C.
Fig. S28. Photos of the S powder, CNT, S cathode, and S/IGCL-NFE.
Fig. S29. PXRD spectra of the IGCL-NFE, CNT, S cathode, and S/IGCL-NFE composite.
Fig. S30. (A, B) SEM images of the S. (C, D) SEM images of the S/IGCL-NFE composite.
Fig. S31. Thermogravimetric curve of S cathode and S/IGCL-NFE cathode.
Fig. S32. DC polarization measurements under electronic blocking conditions for the S and S/IGCL-NFE.
Fig. S33. The GITT curves of S/IGCL-NFE and S.
Fig. S34. Nyquist plots and DRT curves obtained from in situ EIS results during the first discharge of the S and S/IGCL-NFE.
Fig. S35. CV curves of the S/IGCL-NFE and S with a sulfur loading of 4.1 mg cm^{-2} at various scan rates.
Fig. S36. The thickness of the (A) S/IGCL-NFE and (B) S electrode (weight: 100.0 mg) measured by the spiral micrometer.
Fig. S37. CV curves of the S/IGCL-NFE and S with a sulfur loading of 4.1 mg cm^{-2} at 0.1 mV s^{-1}.
Fig. S38. 2D maps of TOF-SIMS of the S/IGCL-NFE and S after discharge at 0.1 C.
Fig. S39. Charge/discharge curves of Li-S cells with the S/IGCL-NFE (A) and S (B) with a sulfur loading of 4.1 mg cm^{-2} at various current densities.
Fig. S40. SEM images showing the cycled Li anode paired with the S/IGCL-NFE (A) and S (B) in Li-S cells. Below are the corresponding S element mappings on the Li anode (C, D). The weak signal of the S element on the surface of cycled S/IGCL-NFE indicates the effective protection effect of the IGCL-NFE (C).
Fig. S41. Cross-sectional SEM image of the S/IGCL-NFE (A, C) and S (B, D) before and after 100 cycles.
Fig. S42. Cycling performance of the Li-S cells with the S/IGCL-NFE at -20 ˚C (S loading: 4.1 mg cm^{-2}).
Fig. S43. Pressure variation diagrams for the Li-S pouch cells with the S and S/IGCL-NFE during the discharging cycle.
Table S1. The key design parameters used for the gravimetric energy density.
Table S2. The calculated gravimetric energy density of Li-S batteries across a range of cathode loading (mg cm^{-2}) (sulfur content=80%, E/S=3.0 μL mg^{-1}, N/P=1.5).
Table S3. The calculated gravimetric energy density of Li-S batteries across a range of sulfur content (wt%) (cathode loading=18.0 mg cm^{-2}, E/S=3.0 μL mg^{-1}, N/P=1.5).

Table S4. The corresponding λ_d for different concentrations of electrolyte.
Table S5. Mass transfer parameters of various species.
Table S6. Kinetic properties of various reactants.
Table S7. Mechanical parameters of various components.
Table S8. Comparison of capacity performance in low-temperature of our Li-S cell based on the S/IGCL-NFE with other reported work.
Table S9. Component details of the Li-S pouch cell with an S loading of 300.0 mg.
Table S10. Component details of the Li-S pouch cell based on the dry electrode (S loading:18.70 mg cm^{-2}).
Table S11. Electrochemical performance under high sulfur loading comparison of our work with previous work.

Supplementary Note 1: Gravimetric energy density analyses of Li-S batteries in a pouch-cell configuration.

The gravimetric energy density of Li-S batteries in a pouch-cell configuration were calculated using the equations below:

$$Gravimetric\ energy\ density = \frac{V_a \times Q_S \times M_C \times wt\%}{M_C + M_{Al} + M_E + M_A + M_{Cu} + M_S + M_P}$$

$$= \frac{V_a \times Q_S \times (\rho_C \times t_C \times wt\%) \times N_C \times A_C}{[(\rho_C \times t_C) + (\rho_{Al} \times t_{Al})] \times N_C \times A_C + \left[(\rho_C \times t_C \times wt\%) \times N_C \times A_C \times R_{\frac{E}{S}} \times \rho_E\right] + [(\rho_A \times t_A) + (\rho_{Cu} \times t_{Cu})] \times N_A \times A_A + (\rho_S \times t_S \times N_S \times A_S) + (\rho_P \times t_P \times N_P \times A_P)}$$

Key design parameters used for the gravimetric energy density analyses are obtained from previous
literature and summarized below in Supplementary Table S1[2]. Dashes are used for variable parameters. Utilizing the equations and specified parameters provided, we calculated the gravimetric energy density of Li-S batteries across a range of cathode loading (mg cm^{-2}) and sulfur content (wt%), as depicted in Table S2, S3, Fig. S1A and B.

Table S1. The key design parameters used for the gravimetric energy density.

Symbol	Value	Unit	Description
V_a	2.1	V	Average output voltage
Q_S	1675.0	mAh g^{-1}	Theoretical specific capacity of sulfur
M_C	-	mg cm^{-2}	Cathode composite loading
M_E	-	g	Weight of the liquid electrolyte
M_{Cu}	4.875	g	Weight of the copper foil
M_{Al}	2.15	g	Weight of the aluminum foil
M_S	1.7	g	Weight of the separator
M_A	-	g	Weight of the Li anode
M_P	2.0	g	Weight of package and tab
Wt%	-	%	Sulfur content in composite electrode
N_C	20	-	Number of cathode layers
N_A	21	-	Number of anode layers
N_P	2	-	Number of Al plastic films
N_S	40	-	Number of separator films
ρ_C	1.38	g cm^{-3}	Cathode density
ρ_A	0.534	g cm^{-3}	Anode density
ρ_S	0.546	g cm^{-3}	Separator density
ρ_E	1.26	g cm^{-3}	Liquid electrolyte density (1M LiTFSI in DOL/DME (1:1))
ρ_{Cu}	8.96	g cm^{-3}	Copper foil density
ρ_{Al}	2.7	g cm^{-3}	Aluminum foil density
ρ_P	1.576	g cm^{-3}	Al plastic film density
t_C	-	μm	Cathode thickness
t_A	-	μm	Anode thickness
t_{Cu}	5.0	μm	Copper foil thickness
t_{Al}	8.0	μm	Aluminum foil thickness
t_P	115.0	μm	Al plastic film thickness
t_S	15.0	μm	Separator thickness
$R_{E/S}$	3.0	μL mg^{-1}	Liquid electrolyte/sulfur ratio
N/P	1.5	-	Negative-to-positive capacity ratio
A_C	50×100	mm^2	Cathode dimension
A_A	52×102	mm^2	Anode dimension
A_P	52×102	mm^2	Packaging materials dimension
A_S	52×102	mm^2	Separator dimension

Table S2. The calculated gravimetric energy density of Li-S batteries across a range of cathode loading (mg cm^{-2}) (sulfur content=80%, E/S=3.0 µL mg^{-1}, N/P=1.5).

Cathode loading (mg cm^{-2})	M_C (g)	M_{Al} (g)	M_E (g)	M_S (g)	M_A (g)	M_{Cu} (g)	M_P (g)	Total weight (g)	Energy density (Wh kg^{-1})
3.0	7.5	2.15	22.68	1.70	4.36	4.875	2.0	45.10	467.96
6.0	15.0	2.15	45.36	1.70	8.73	4.875	2.0	79.68	529.74
9.0	22.5	2.15	68.04	1.70	13.08	4.875	2.0	114.26	554.13
12.0	30.0	2.15	90.72	1.70	17.44	4.875	2.0	148.88	567.03
15.0	37.5	2.15	113.40	1.70	21.80	4.875	2.0	183.42	575.31
18.0	45.0	2.15	136.08	1.70	26.20	4.875	2.0	218.00	580.80

Table S3. The calculated gravimetric energy density of Li-S batteries across a range of sulfur content (wt%) (cathode loading=18.0 mg cm^{-2}, E/S=3.0 µL mg^{-1}, N/P=1.5).

Sulfur content (%)	M_C (g)	M_{Al} (g)	M_E (g)	M_S (g)	M_A (g)	M_{Cu} (g)	M_P (g)	Total weight (g)	Energy density (Wh kg^{-1})
30	120.0	2.15	136.08	1.70	26.20	4.875	2.0	293.00	432.18
40	90.0	2.15	136.08	1.70	26.20	4.875	2.0	263.00	481.48
50	72.0	2.15	136.08	1.70	26.20	4.875	2.0	245.00	516.85
60	60.0	2.15	136.08	1.70	26.20	4.875	2.0	233.00	543.47
70	51.4	2.15	136.08	1.70	26.20	4.875	2.0	224.40	564.30
80	45.0	2.15	136.08	1.70	26.20	4.875	2.0	218.00	580.80

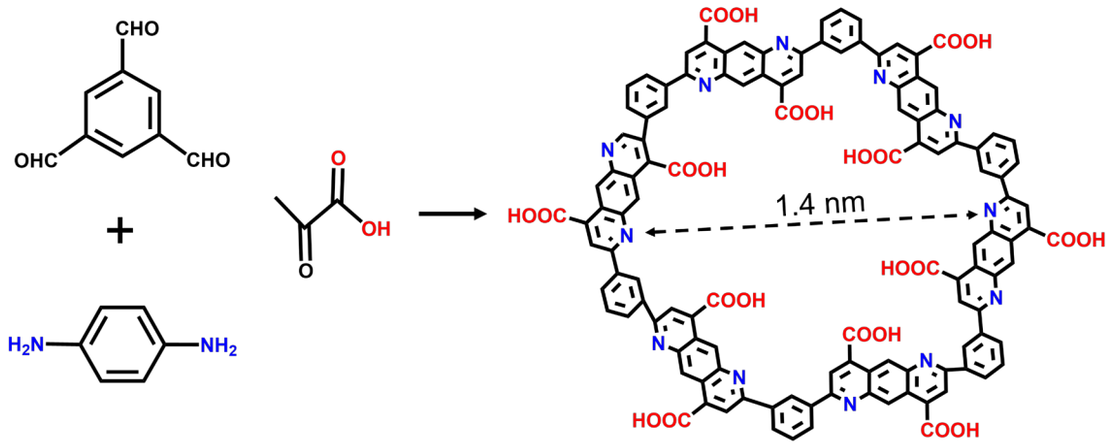

Fig. S1. Synthesis of 4-carboxyl-quinoline linked covalent organic frameworks using a one-pot Doebner reaction.

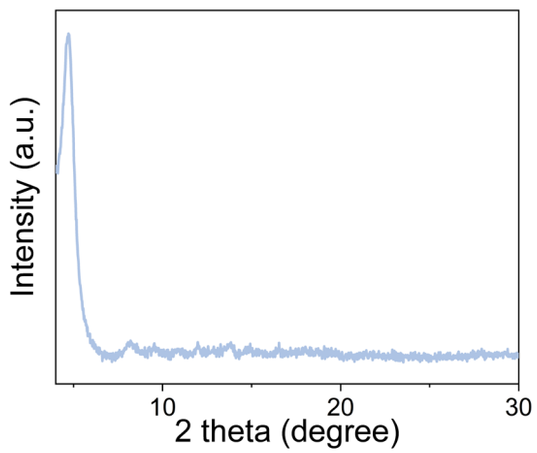

Fig. S2. PXRD spectra of the 4-carboxyl-quinoline linked covalent organic frameworks.

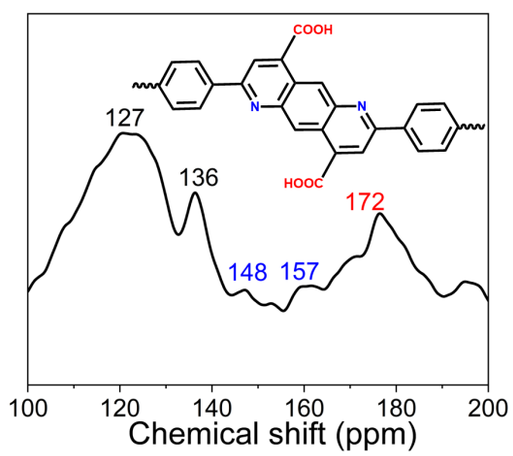

Fig. S3. The ^{13}C NMR spectra of the 4-carboxyl-quinoline linked covalent organic frameworks.

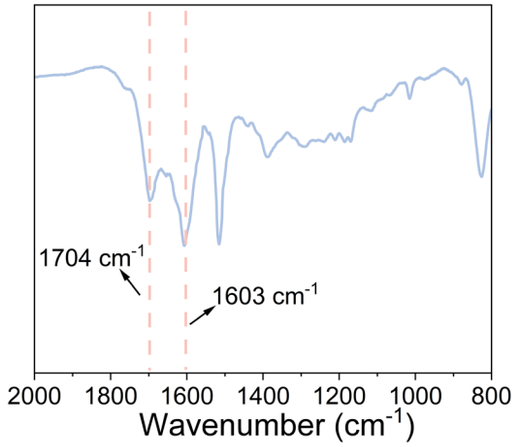

Fig. S4. IR spectra of the 4-carboxyl-quinoline linked covalent organic frameworks.

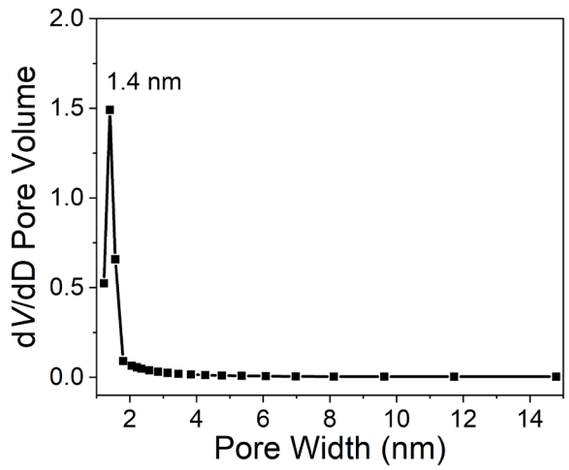

Fig. S5. Pore size distribution of the 4-carboxyl-quinoline linked covalent organic frameworks.

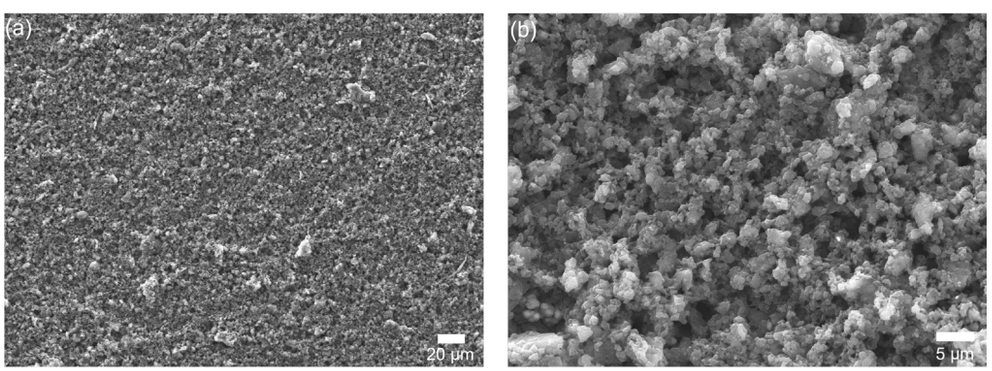

Fig. S6. SEM images of the 4-carboxyl-quinoline linked covalent organic frameworks.

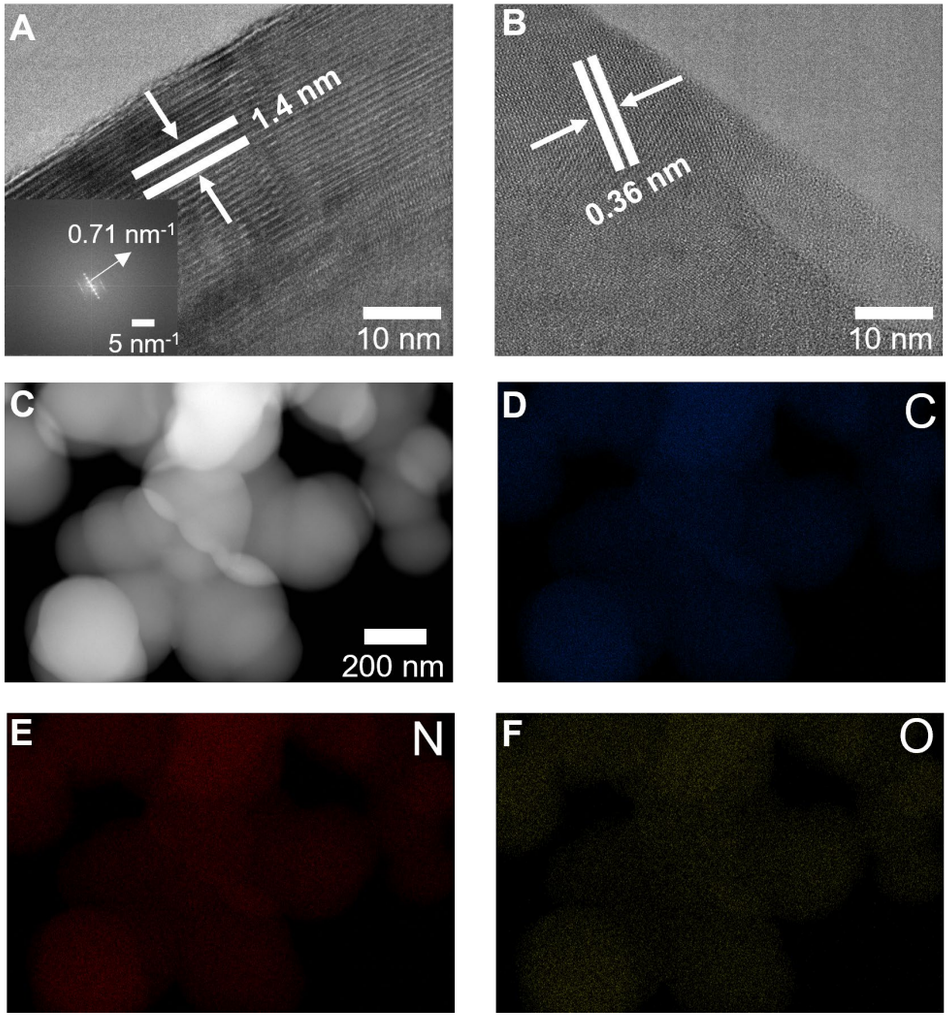

Fig. S7. (A, B) HR-TEM images and (C-F) EDX mapping of 4-carboxyl-quinoline linked covalent organic frameworks. The interplanar d spacing of ~0.36 nm was corresponding to the 001 lattice plane.

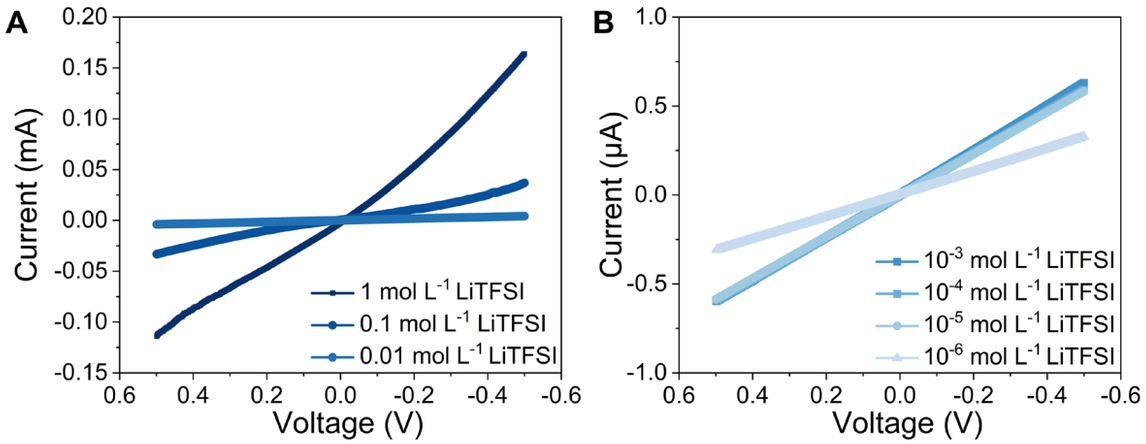

Fig. S8. The typical I-V curves of the IGCL-NFE at different LiTFSI concentrations.

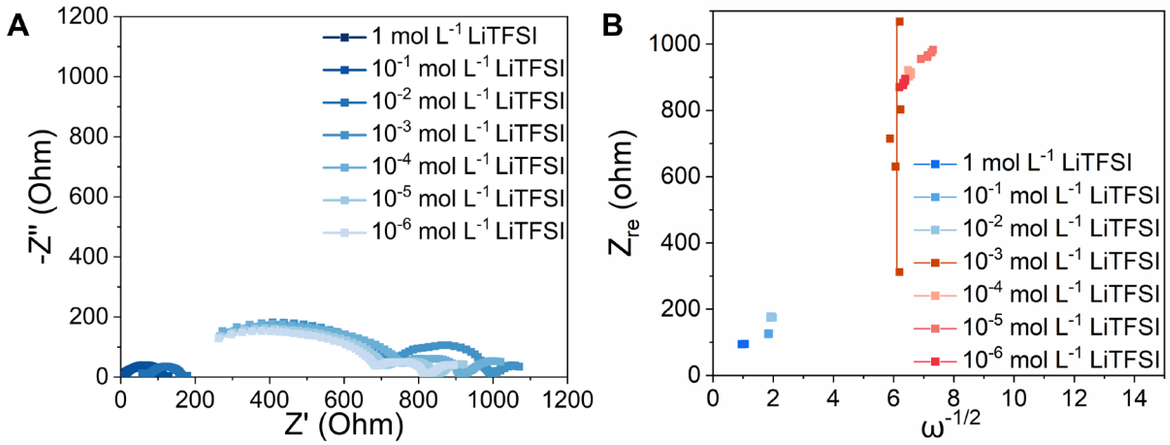

Fig. S9. (A) EIS spectra of the IGCL-NFE at different LiTFSI concentrations. (B) Relationship plot of impedance as a function of the inverse square root of the angular frequency for the calculation of Li^+ diffusion coefficient.

The Li^+ diffusion coefficient was calculated based on the EIS measurement according to the following equations[3]:

$$D_{Li^+} = \frac{R^2T^2}{2n^4F^4A^2C^2\sigma^2} \tag{S1}$$

Where R (8.314 J mol^{-1} K^{-1}), F (96500 C mol^{-1}), and T (298.15 K) were respectively ideal gas constant, Faraday constant, and the absolute temperature, A represented the area of the electrode (1.13 cm^2), n was the number of electrons per molecule during oxidization and C was the concentration of Li^+, σ represented the Warburg factor that could be calculated from the relationship of Z_{re} versus $\omega^{-1/2}$.

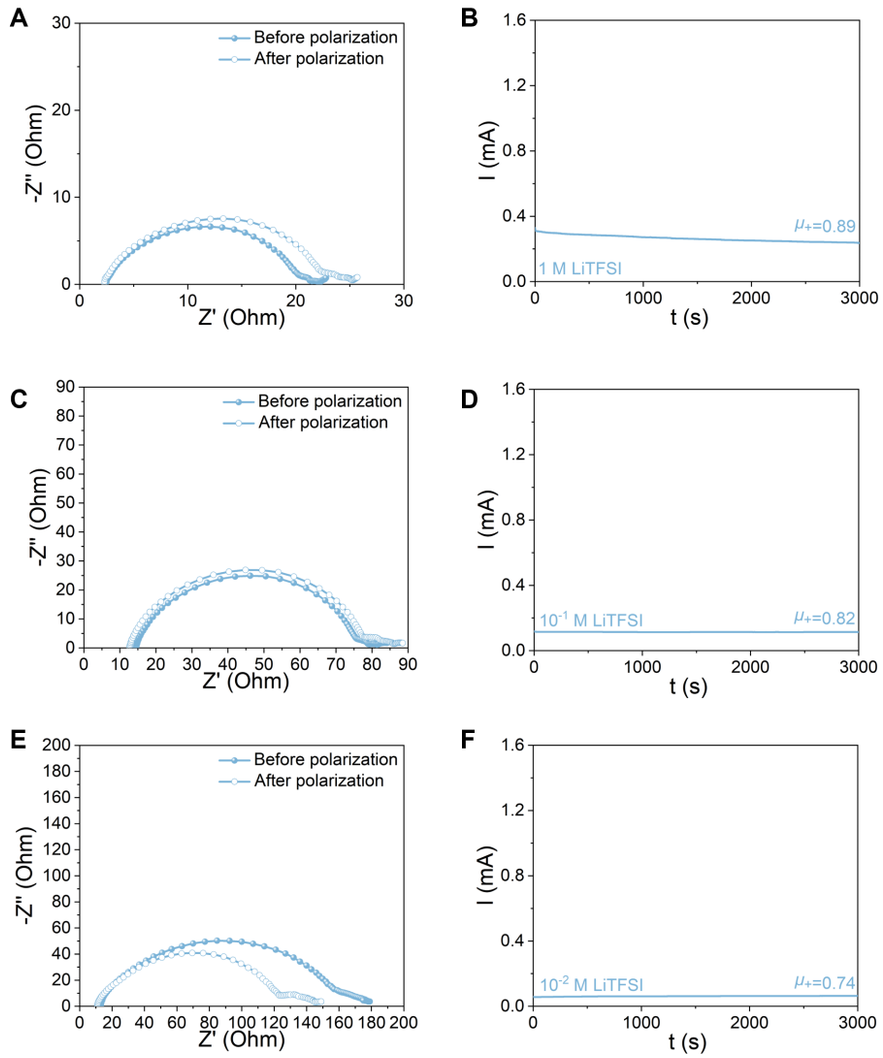

Fig. S10. (A, C and E) EIS curves of the Li//Li symmetric cells with IGCL-NFE at initial and steady states at various concentrations of LiTFSI (From 1 mol L^{-1} LiTFSI to 10^{-2} mol L^{-1} LiTFSI), and the corresponding Polarization curves (B, D and F).

Li^+ transfer number (μ_+) was measured by AC impedance and DC polarization measurements using a Li-Li symmetric cell and calculated using the following equation[3]:

$$\mu_+ = \frac{I_{ss}(\Delta V - I_0 R_0)}{I_0(\Delta V - I_{ss} R_{ss})} \tag{S2}$$

Where R_0 and R_s are the initial and steady resistances (Ω) of the interfacial layers of the electrolyte and Li metal electrode, respectively. They were obtained before and after polarization from the impedance spectra of the cell with an oscillation voltage of 5 mV (frequency between 10 MHz and 1 MHz). In addition, the initial (I_o) and steady (I_s) current flow through the cell was measured by DC polarization with a voltage ((ΔV= 10 mV). The detailed tests were described in previous studies.

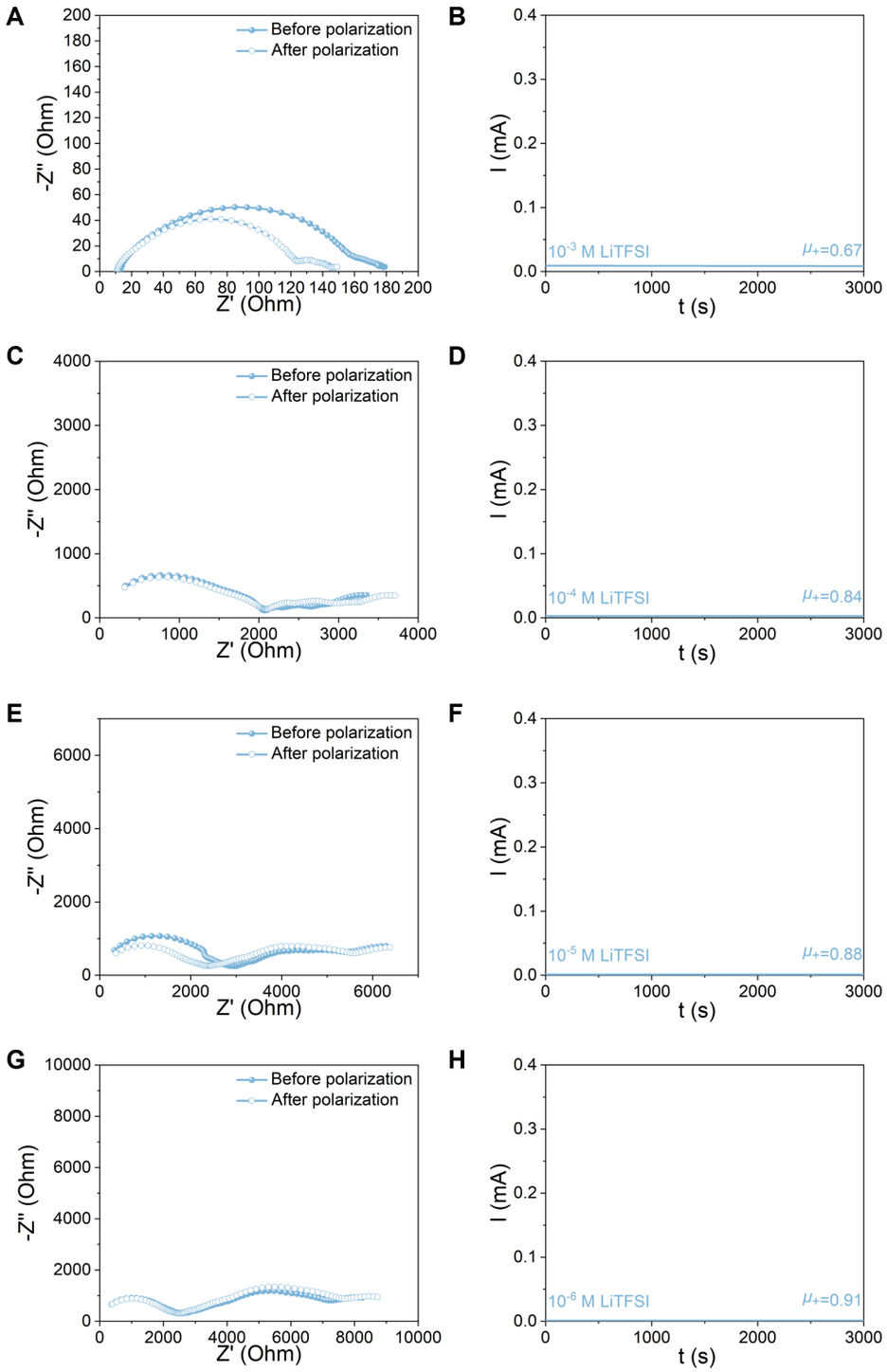

Fig. S11. (A, C, E and G) EIS curves of the Li//Li symmetric cells with IGCL-NFE at initial and steady states at various concentrations of LiTFSI (From 10^{-3} mol L^{-1} to 10^{-6} mol L^{-1} LiTFSI), and the corresponding Polarization curves (B, D, F and H).

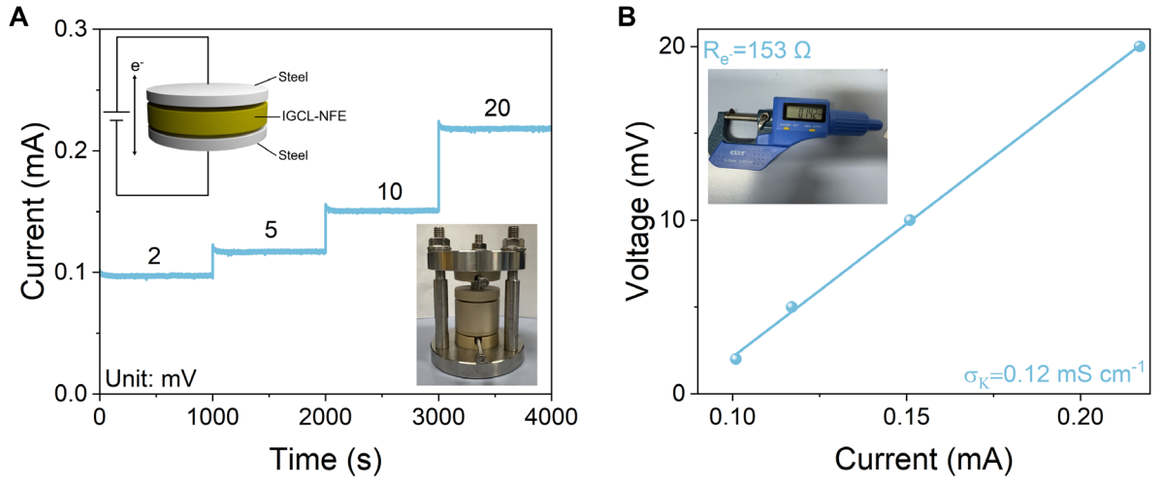

Fig. S12. (**A**) DC polarization measurements under ionic blocking conditions for IGCL-NFE. (**B**) Effective electronic conductivity determined by DC polarization.

The effective electronic conductivity of IGCL-NFE was measured using an ion-blocking symmetric cell configuration. 50.0 mg of powders were loaded within a PEEK cylinder with an inner diameter of 10 mm and cold-pressed at a pressure of 300 MPa for 1 min. The thickness of the pellet was measured as 0.142 mm for IGCL-NFE with a spiral micrometer after measurement. After resting for 1 h under open circuit conditions, the applied potentials were applied in the following sequence: +2, +5, +10, and +20 mV, each maintained for an equilibration period of 20 mins.

The electronic resistance of the composite cathode can be calculated using Ohm's Law (R_k, where k = e^-). By integrating the current response under varied voltages, the geometric area (A = 0.785 cm^2), and the thickness of the electrode, the effective electronic conductivity (σ_k) within the IGCL-NFE can be calculated using Equation[4]:

$$\sigma_k = \frac{d}{AR_k} \tag{S3}$$

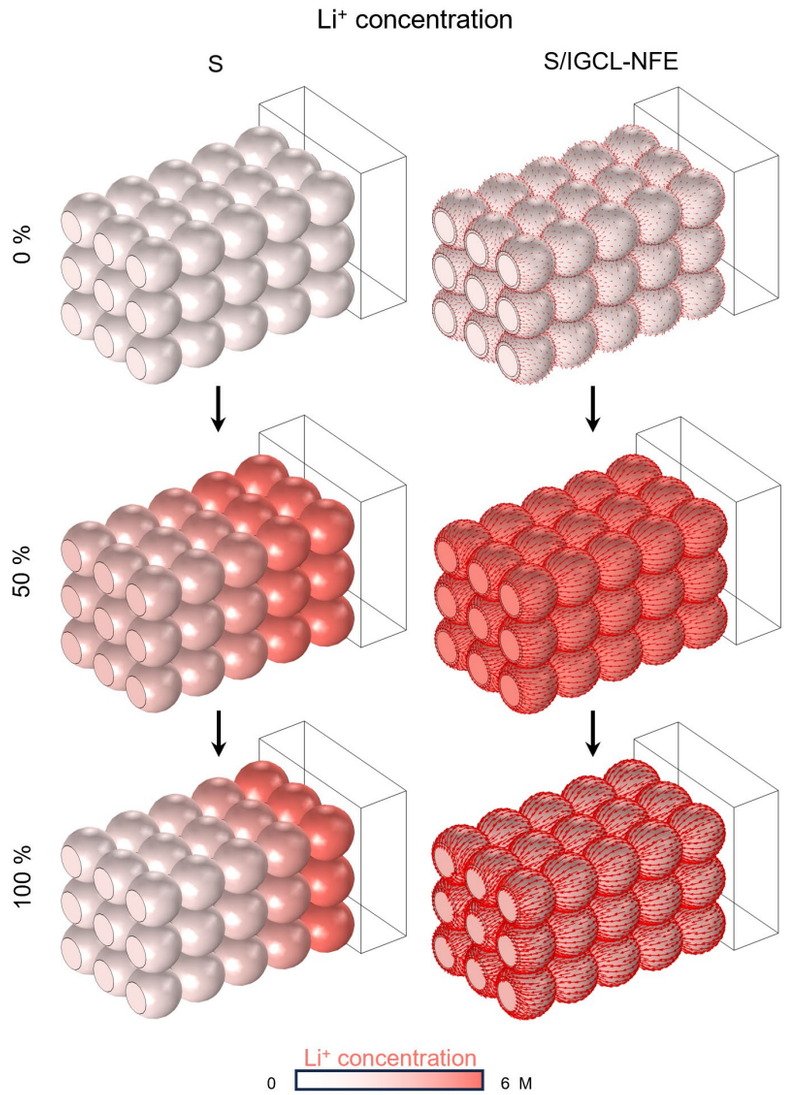

Fig. S13. Local Li^+ concentration distributions for the Li_2S-forming reaction in the bare S and S/IGCL-NFE models with a current density of 2 C at 25 ˚C.

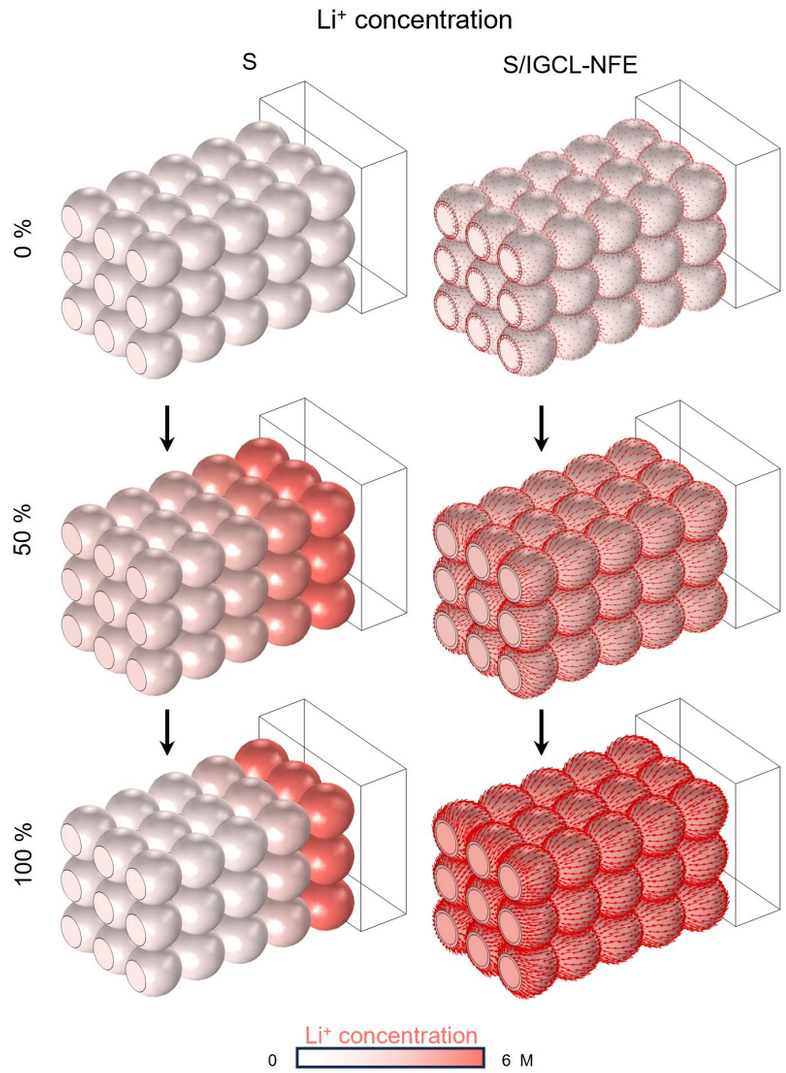

Fig. S14. Local Li^+ concentration distributions for the Li_2S-forming reaction in the bare S and S/IGCL-NFE models with a current density of 5 C at 25 ˚C.

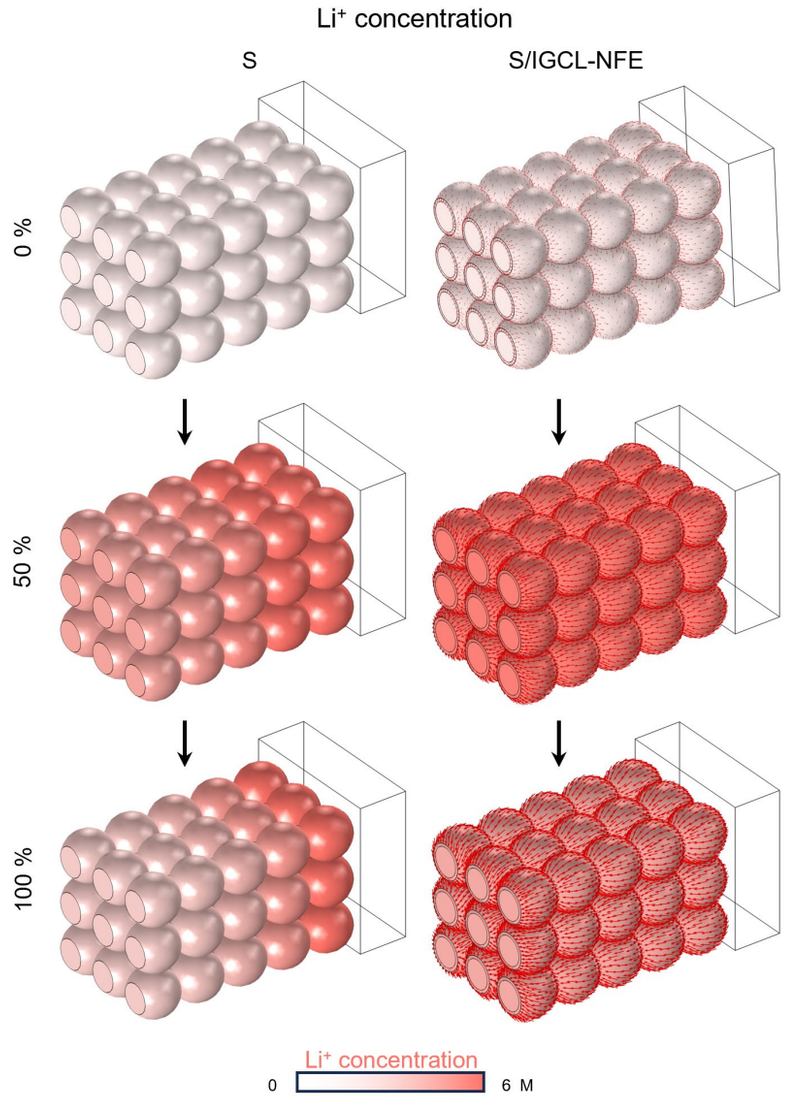

Fig. S15. Local Li^+ concentration distributions for the Li_2S-forming reaction in the bare S and S/IGCL-NFE models with a current density of 1 C at -20 ˚C.

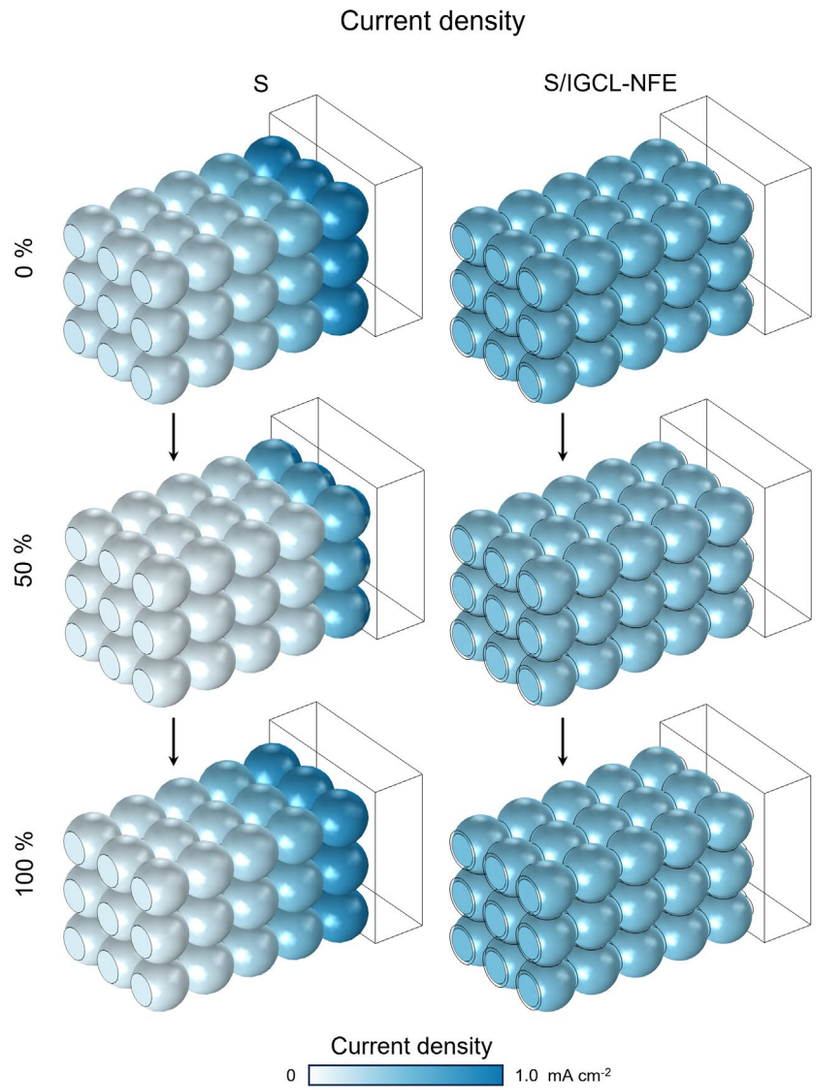

Fig. S16. Local current density distributions for the Li_2S-forming reaction in the bare S and S/IGCL-NFE models with a current density of 2 C at 25 ˚C.

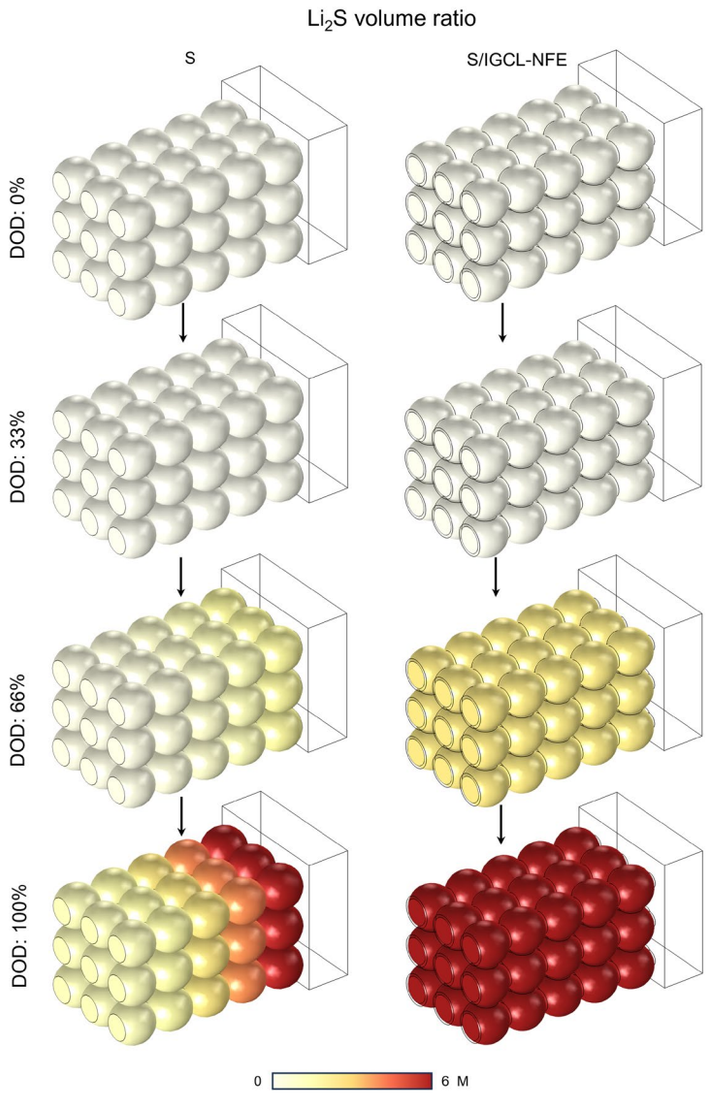

Fig. S17. Simulation of the cathode utilization evolution in the bare S and S/IGCL-NFE models from 0% depth of charge (DOD) to 100% DOD with a current density of 2 C at 25 ˚C.

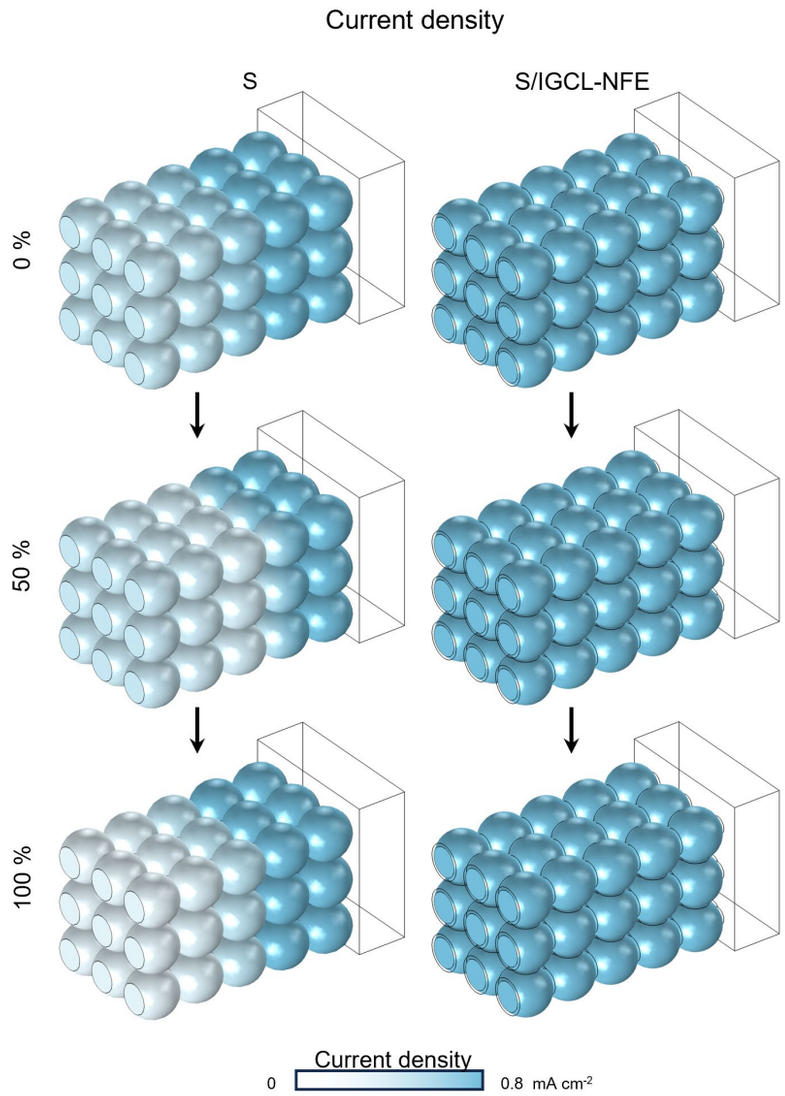

Fig. S18. Local current density distributions for the Li_2S-forming reaction in the bare S and S/IGCL-NFE models with a current density of 5 C at 25 ˚C.

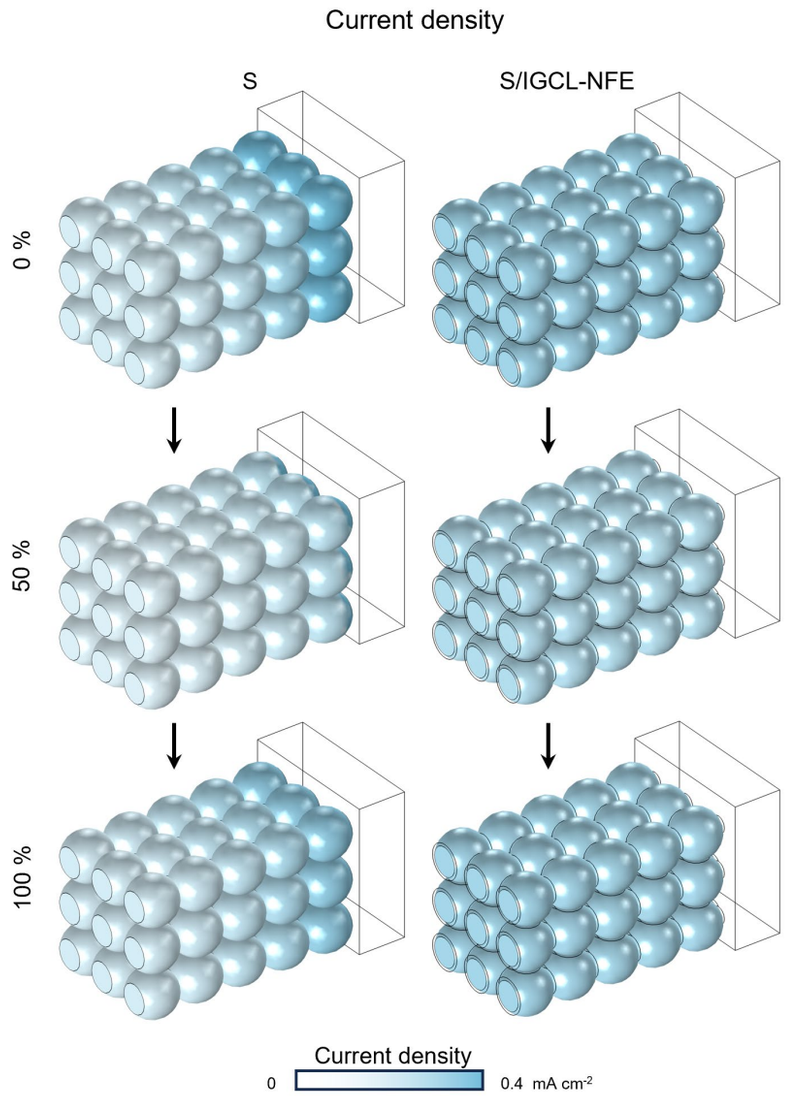

Fig. S19. Local current density distributions for the Li_2S-forming reaction in the bare S and S/IGCL-NFE models with a current density of 1 C at -20 ˚C.

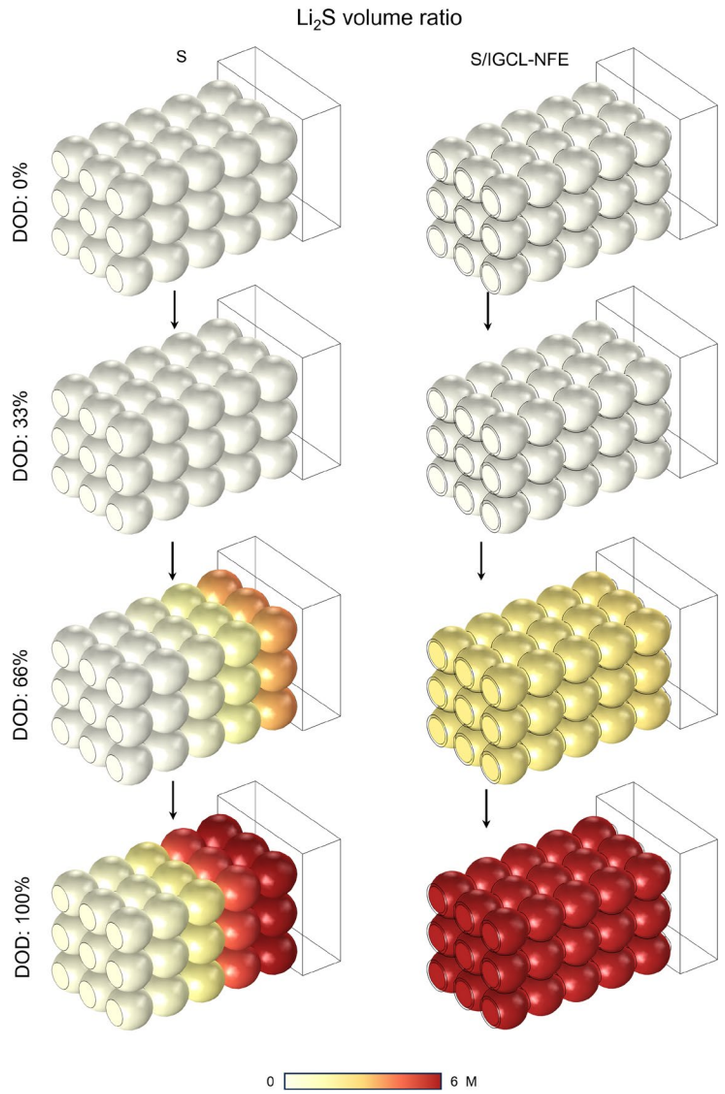

Fig. S20. Simulation of the cathode utilization evolution in the bare S and S/IGCL-NFE models from 0% depth of charge (DOD) to 100% DOD with a current density of 5 C at 25 ˚C.

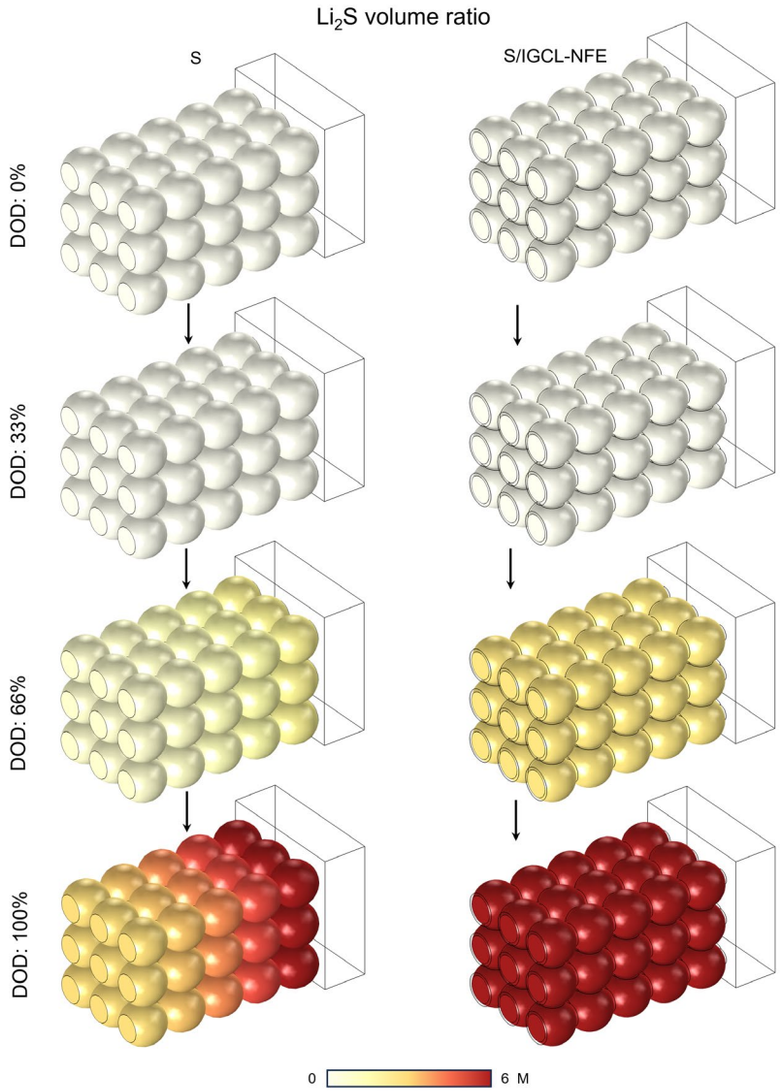

Fig. S21. Simulation of the cathode utilization evolution in the bare S and S/IGCL-NFE models from 0% depth of charge (DOD) to 100% DOD with a current density of 1 C at -20 ˚C.

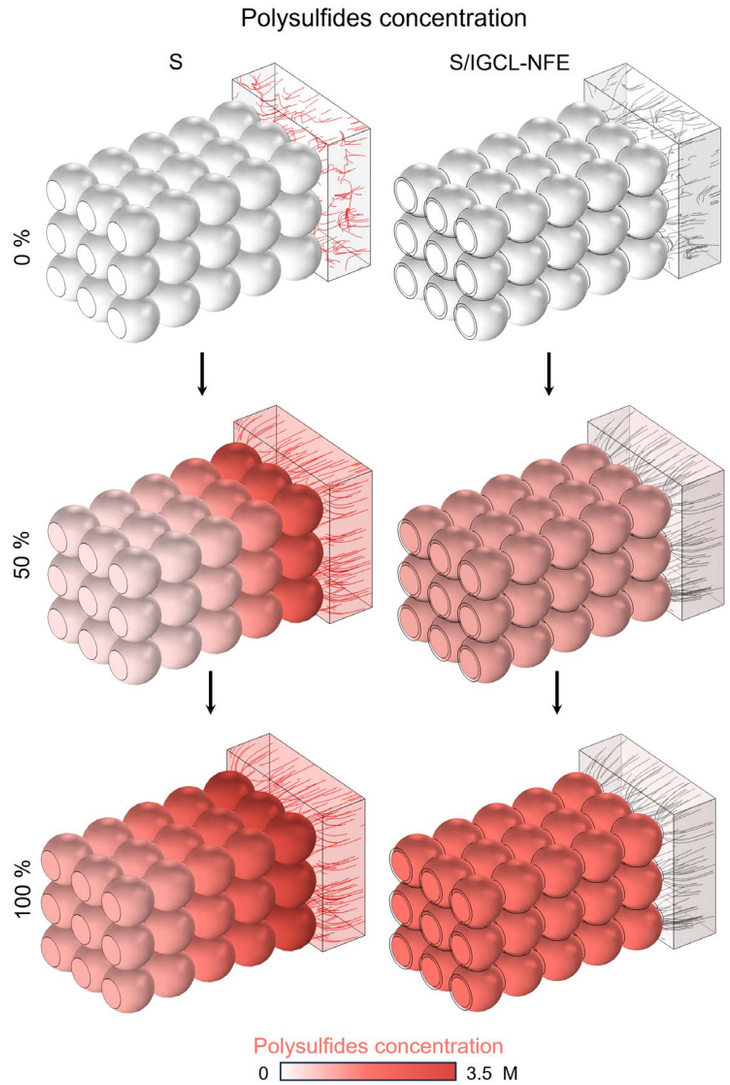

Fig. S22. Polysulfides distributions for the Li_2S-forming reaction in the bare S and S/IGCL-NFE models with a current density of 2 C at 25 ˚C.

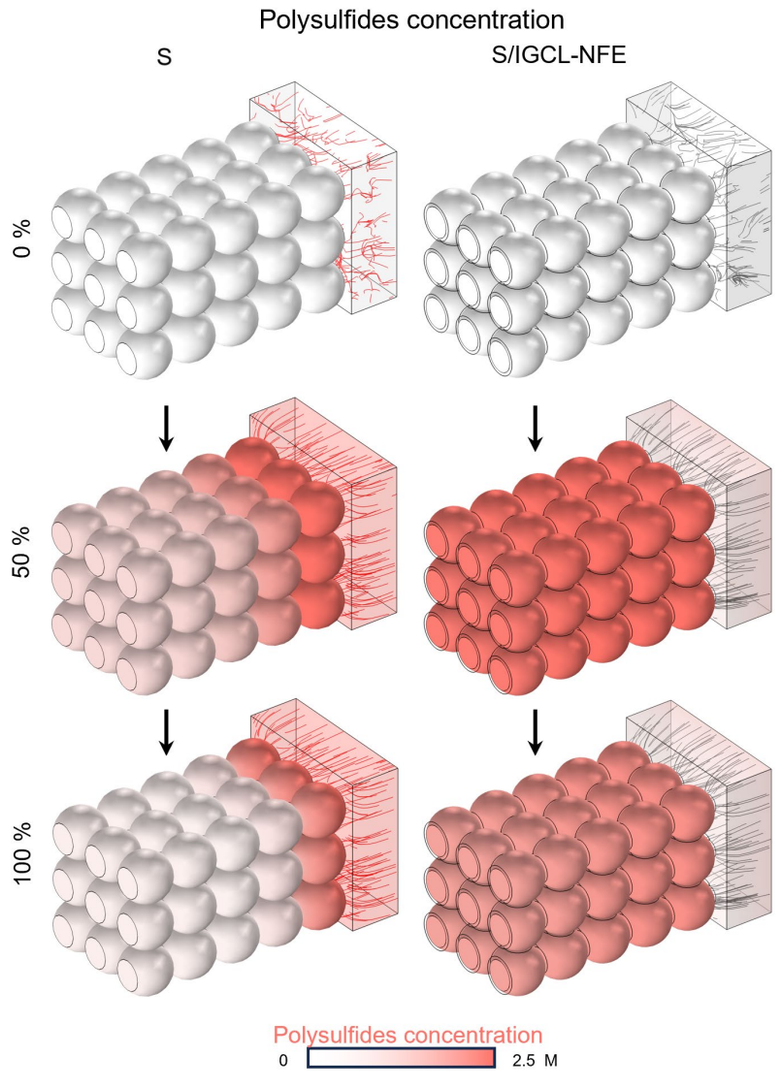

Fig. S23. Polysulfides distributions for the Li_2S-forming reaction in the bare S and S/IGCL-NFE models with a current density of 5 C at 25 ˚C.

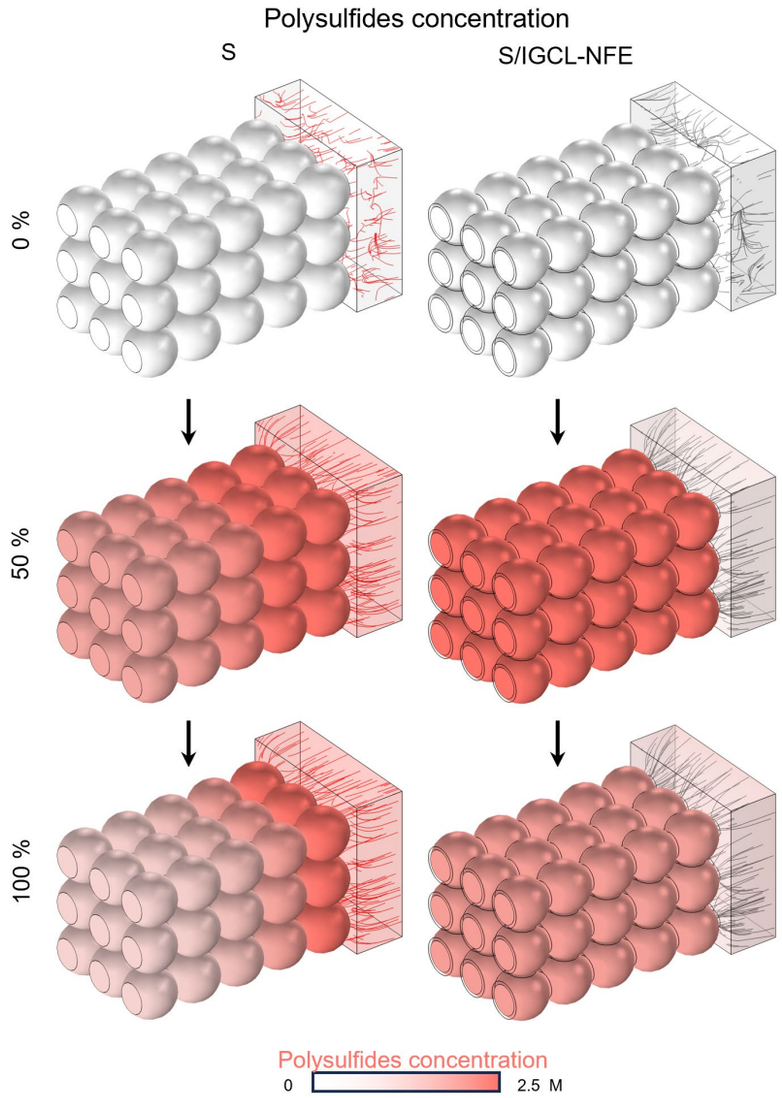

Fig. S24. Polysulfides distributions for the Li_2S-forming reaction in the bare S and S/IGCL-NFE models with a current density of 1 C at -20 ˚C.

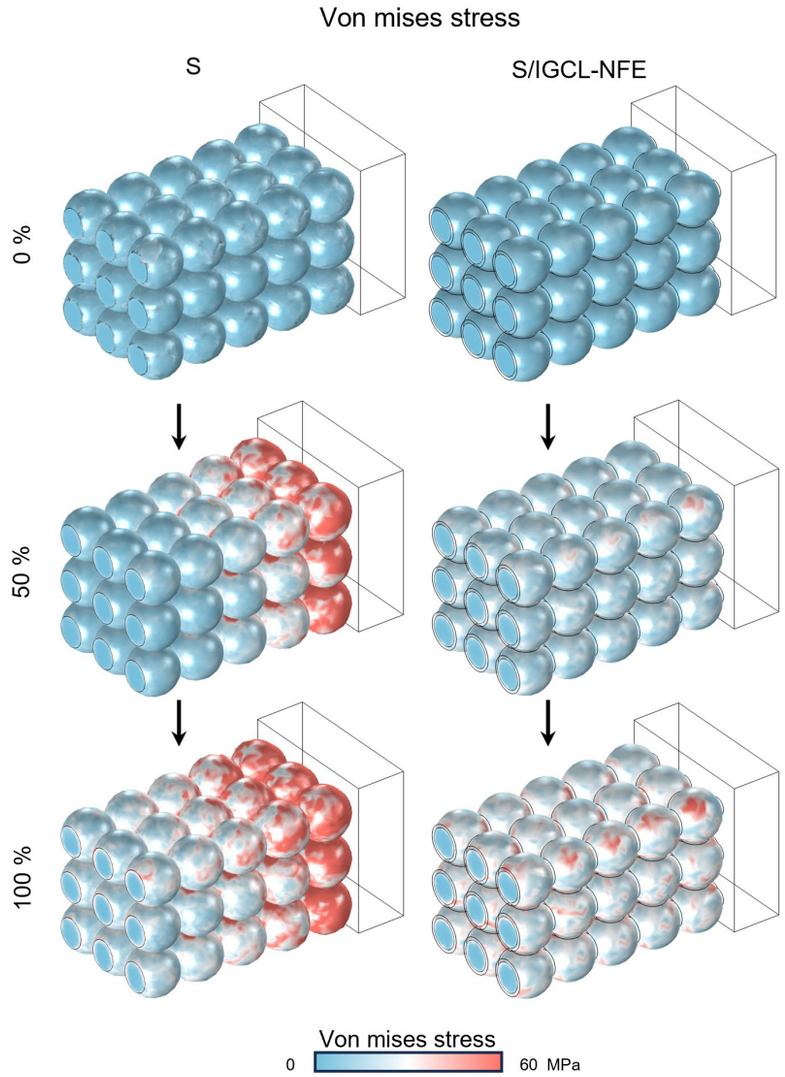

Fig. S25. Simulated electrode expansion stress after S_8 was converted into Li_2S in the bare S and S/IGCL-NFE models with a current density of 2 C at 25 ˚C.

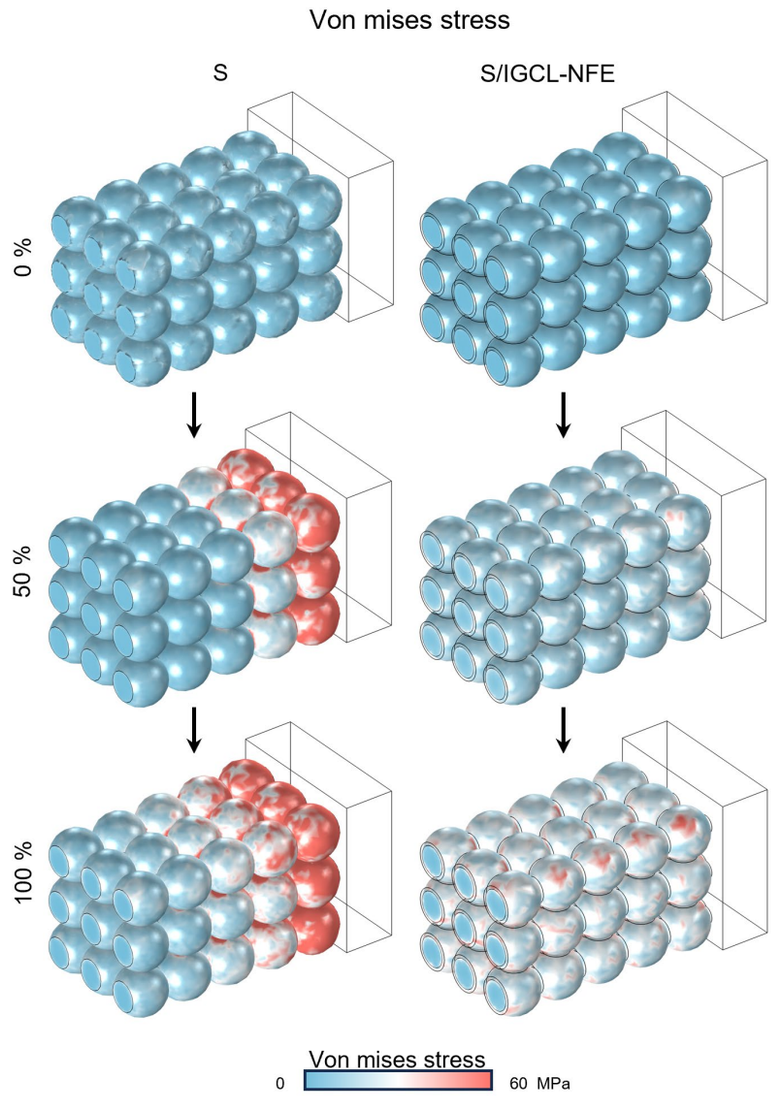

Fig. S26. Simulated electrode expansion stress after S_8 was converted into Li_2S in the bare S and S/IGCL-NFE models with a current density of 5 C at 25 ˚C.

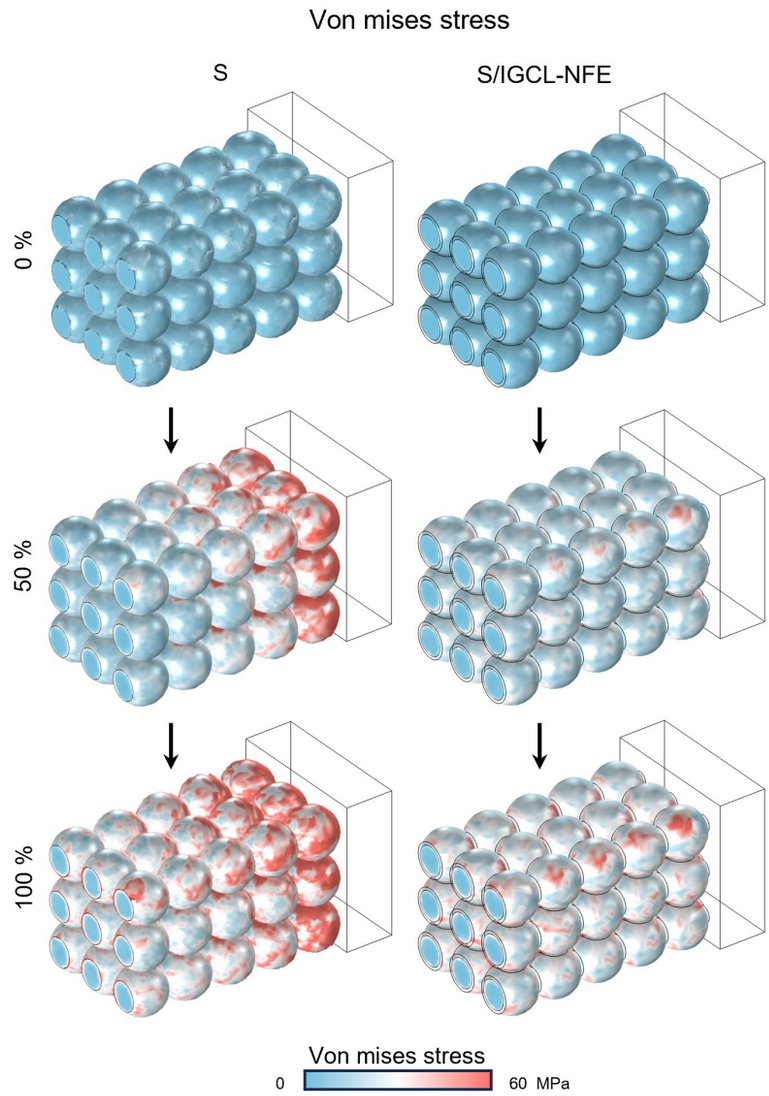

Fig. S27. Simulated electrode expansion stress after S_8 was converted into Li_2S in the bare S and S/IGCL-NFE models with a current density of 1 C at -20 ˚C.

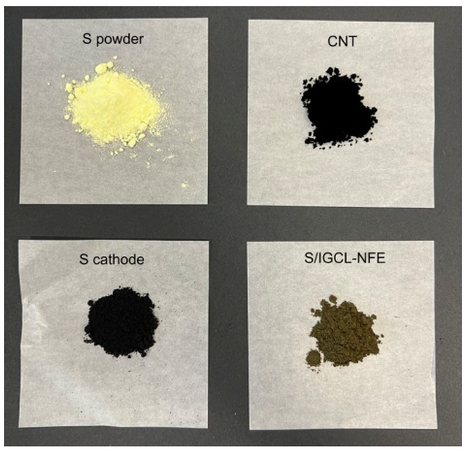

Fig. S28. Photos of the S powder, CNT, S cathode, and S/IGCL-NFE composite.

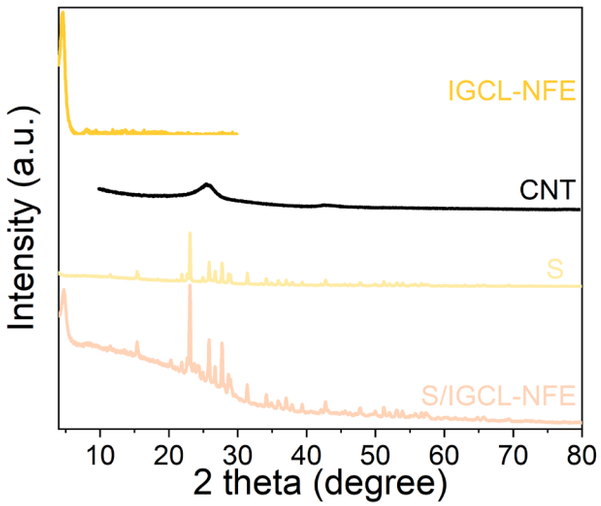

Fig. S29. PXRD spectra of the IGCL-NFE, CNT, S cathode, and S/IGCL-NFE composite.

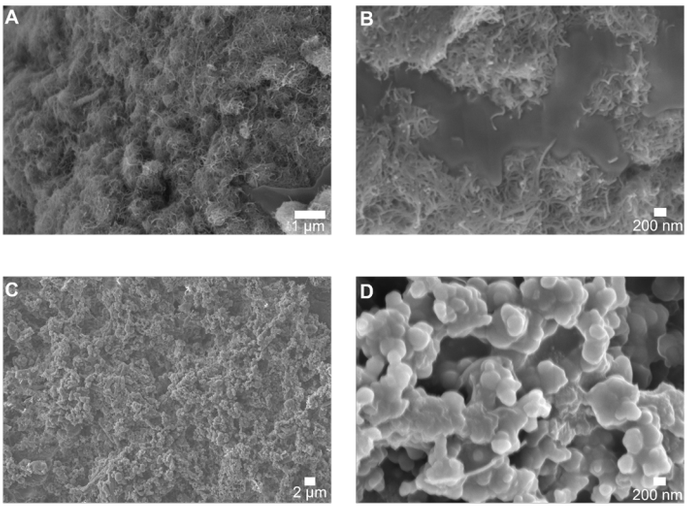

Fig. S30. (A, B) SEM images of the S. (C, D) SEM images of the S/IGCL-NFE composite.

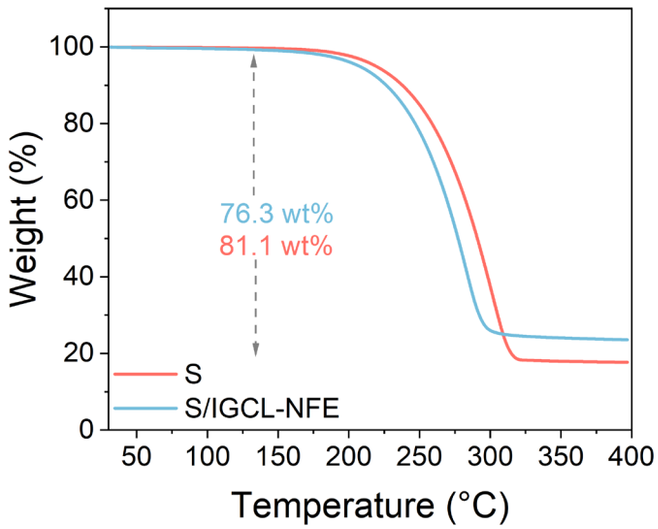

Fig. S31. Thermogravimetric curves of S cathode and S/IGCL-NFE cathode.

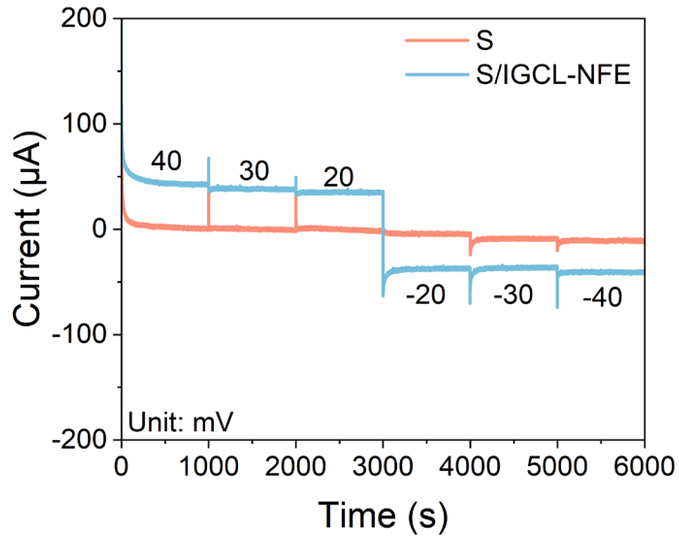

Fig. S32. DC polarization measurements under electronic blocking conditions for the S and S/IGCL-NFE.

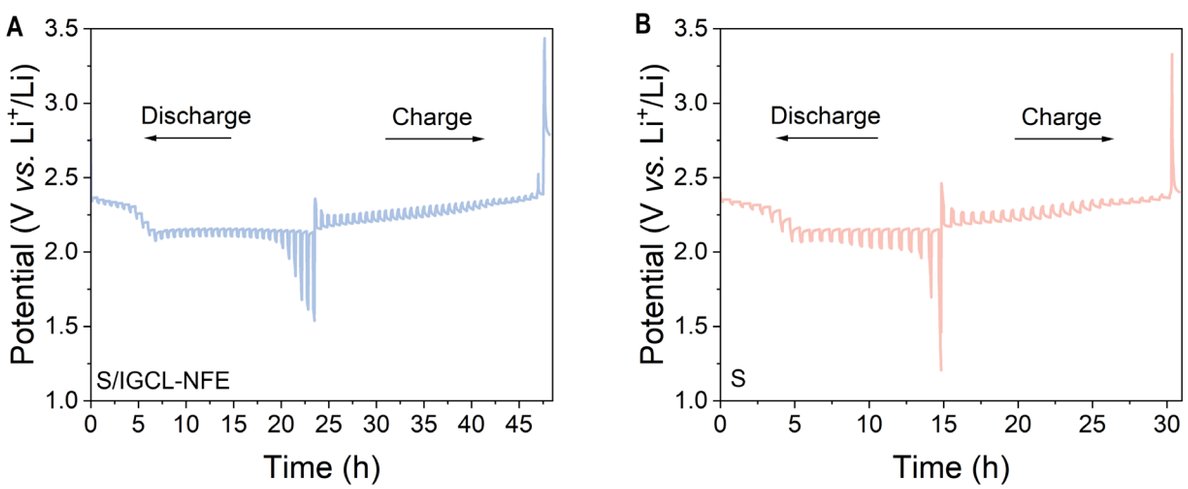

Fig. S33. GITT curves of the S/IGCL-NFE and S.

The GITT is one method to obtain D_{Li^+} based on a simplified Fick's second law[5]:

$$D_{Li^+} = \frac{4}{\pi\tau}\left(\frac{n_M V_M}{S}\right)^2\left(\frac{\Delta E_s}{\Delta E_\tau}\right)^2 \tag{S4}$$

Where τ represents the relaxation time (30 mins), n_M denotes the moles, V_M stands for the molar volume of the electrode material, S is the electrode area (1.13 cm^2), ΔE_s is the steady-voltage change after 30 mins of relaxation, and ΔE_τ is the change in the transient-voltage change after 10 mins discharge or charge process at 0.1 C.

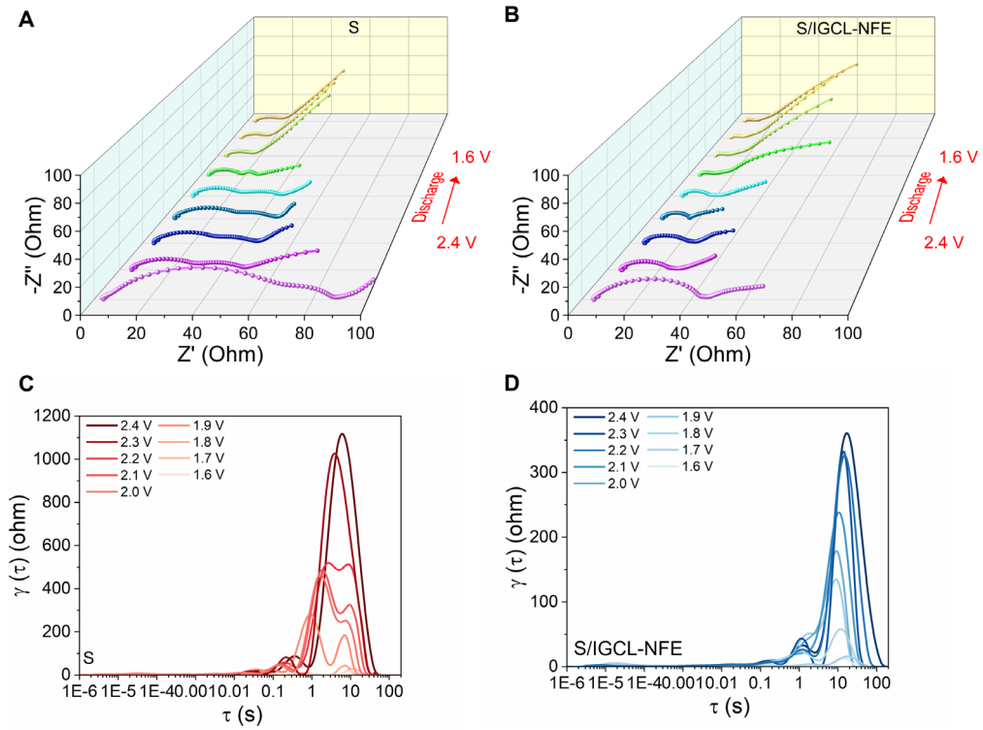

Fig. S34. Nyquist plots and DRT curves obtained from in situ EIS results during the first discharge of the S and S/IGCL-NFE.

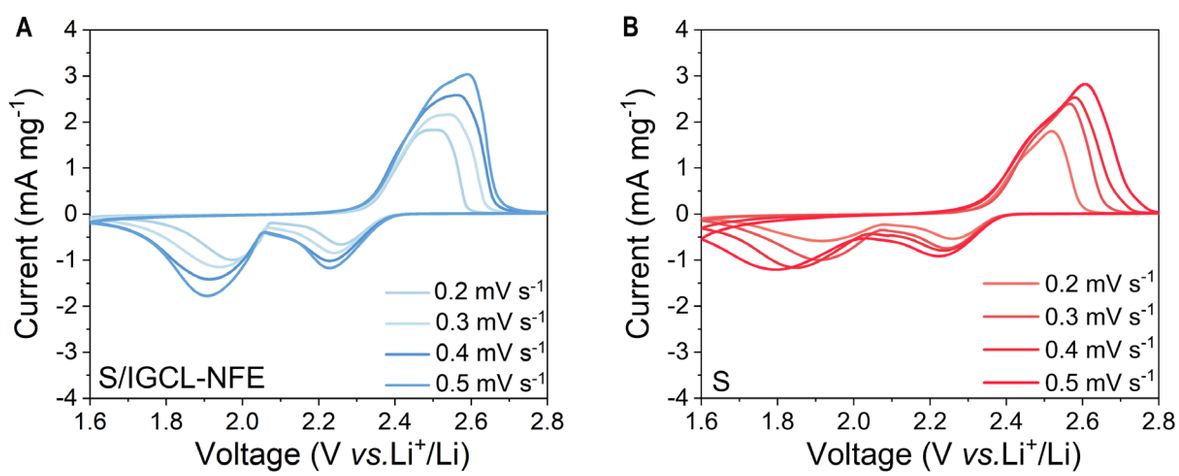

Fig. S35. CV curves of the S/IGCL-NFE and S with a sulfur loading of 4.1 mg cm^{-2} at various scan rates.

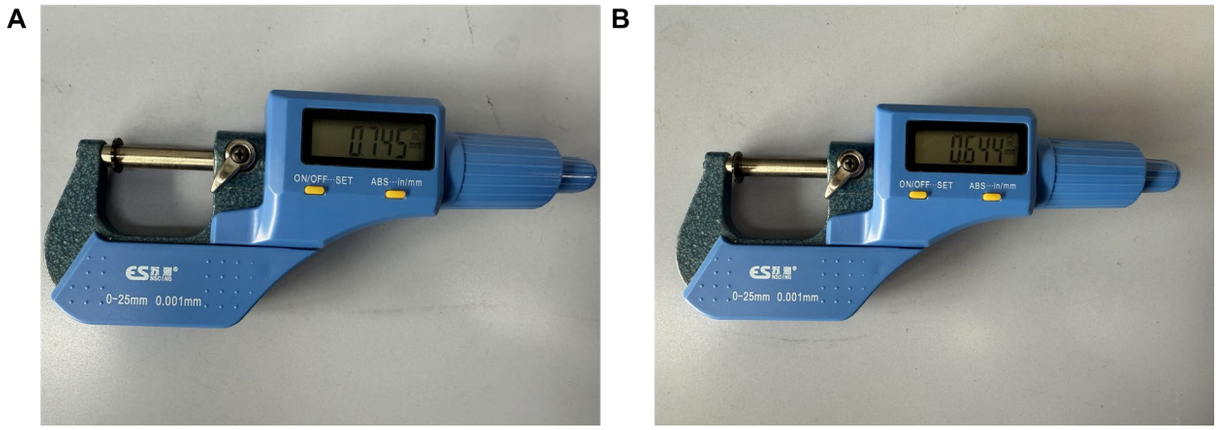

Fig. S36. The thickness of the (A) S/IGCL-NFE and (B) S electrode (weight: 100.0 mg) measured by the spiral micrometer.

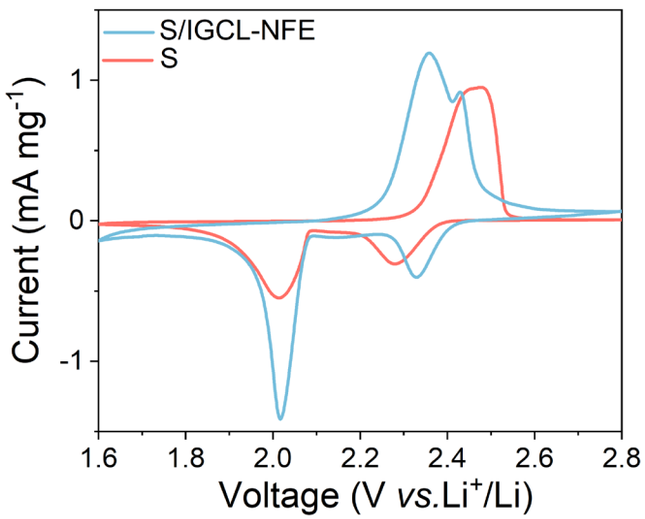

Fig. S37. CV curves of the S/IGCL-NFE and S with a sulfur loading of 4.1 mg cm^{-2} at 0.1 mV s^{-1}.

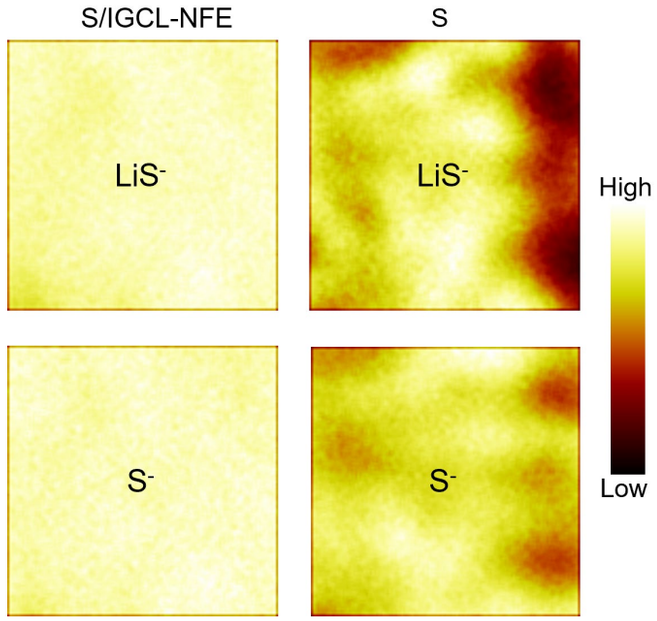

Fig. S38. 2D maps of TOF-SIMS of the S/IGCL-NFE and S after discharge at 0.1 C.

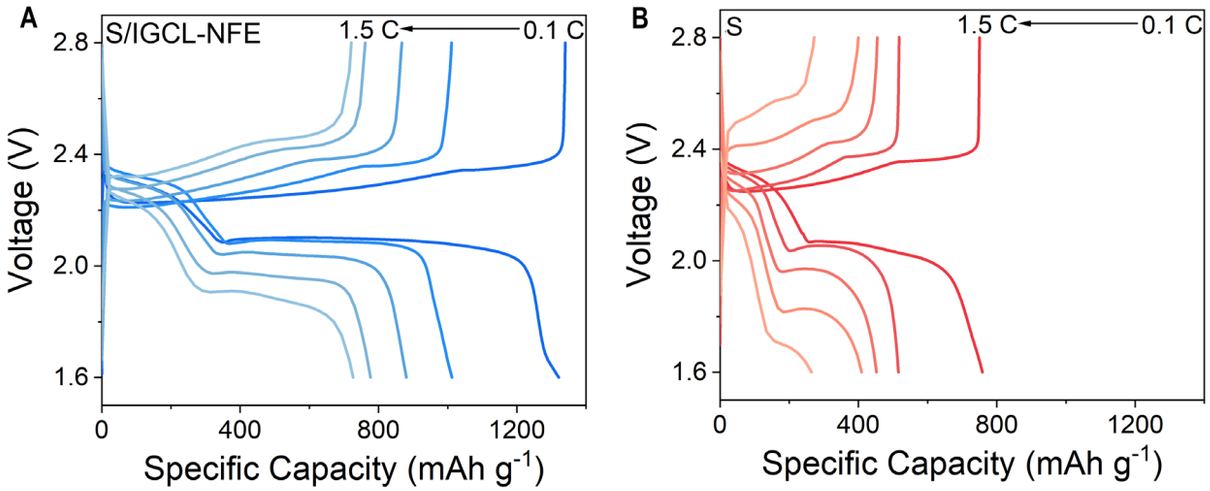

Fig. S39. Charge/discharge curves of Li-S cells with the S/IGCL-NFE (A) and S (B) with a sulfur loading of 4.1 mg cm^{-2} at various current densities.

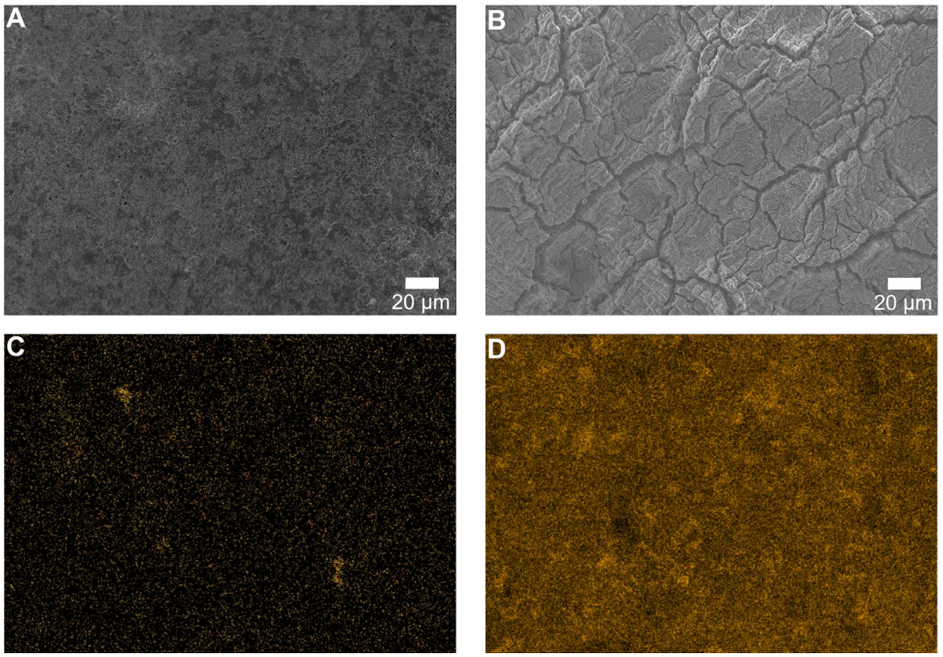

Fig. S40. SEM images showing the cycled Li anode paired with the S/IGCL-NFE (A) and S (B) in Li-S cells. Below are the corresponding S element mappings on the Li anode (C, D). The weak signal of the S element on the surface of cycled S/IGCL-NFE indicates the effective protection effect of the IGCL-NFE (C).

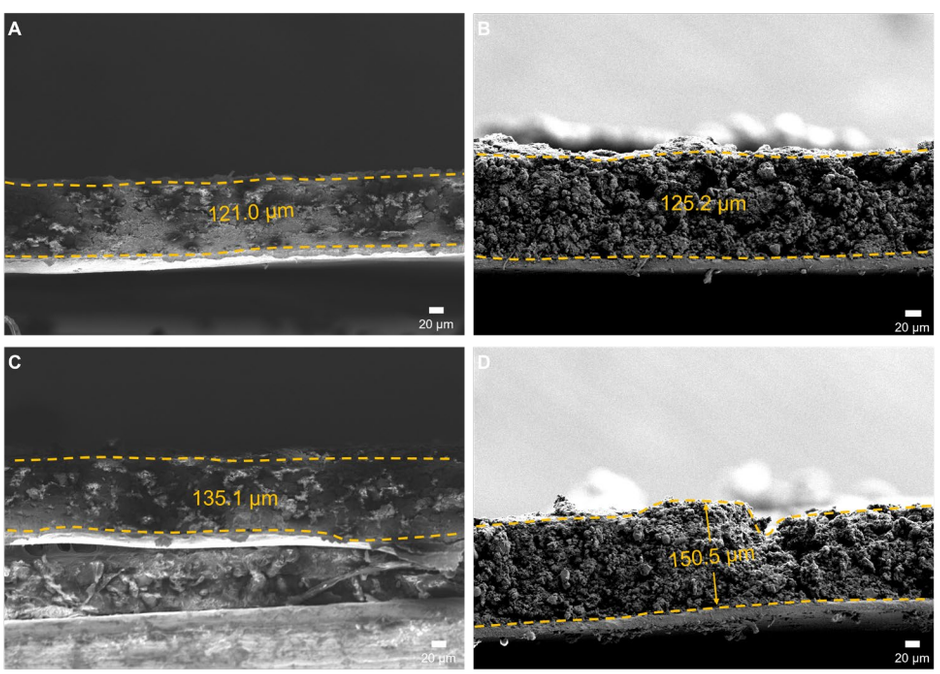

Fig. S41. Cross-sectional SEM images of the S/IGCL-NFE (A, C) and S (B, D) before and after 100 cycles.

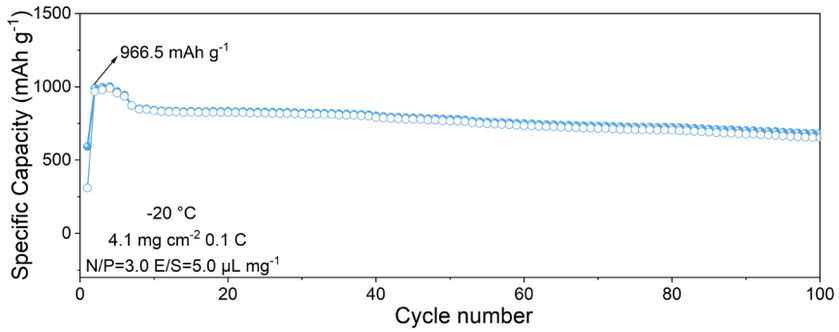

Fig. S42. Cycling performance of the Li-S cell with the S/IGCL-NFE at -20 °C (S loading: 4.1 mg cm^{-2}).

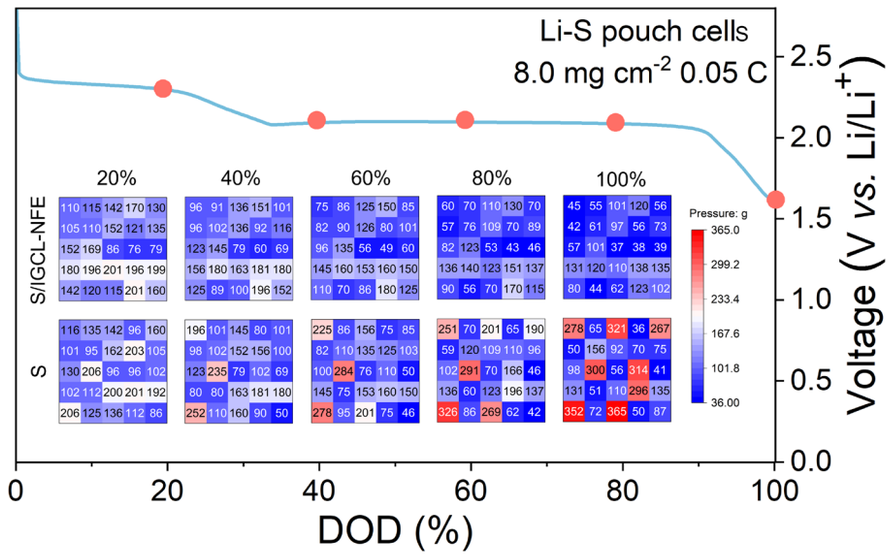

Fig. S43. Pressure variation diagrams for the Li-S pouch cells with the S and S/IGCL-NFE during the discharging cycle.

Table S4. The corresponding λ_d for different concentrations of electrolyte.

C (LiTFSI) (mol L^{-1})	λ_d (nm)
1	0.09
10^{-1}	0.28
10^{-2}	0.89
10^{-3}	2.86
10^{-4}	9.05
10^{-5}	28.60
10^{-6}	95.30

Table S5. Mass transfer parameters of various species.

Species	C_{ref} (mol m^{-3})	D_0 (m^2 s^{-1})	z
Li^+	1.00×10^{3}	1.00×10^{-10}	1
A^-	1.00×10^{3}	4.00×10^{-10}	-1
S^{2-}	8.27×10^{-10}	1.00×10^{-10}	-2
S_2^{2-}	5.23×10^{-7}	1.00×10^{-10}	-2
S_4^{2-}	2.00×10^{-2}	1.00×10^{-10}	-2
S_6^{2-}	3.24×10^{-1}	6.00×10^{-10}	-2
S_8^{2-}	1.78×10^{-1}	6.00×10^{-10}	-2
S_8	1.90×10^{1}	1.00×10^{-9}	0

Table S6. Kinetic properties of various reactants.

Reactions	E_{eq} (V)	$I_{0,ref}$ (A m^{-2})	n
$Li^+ + e^- \rightleftharpoons Li$	0.000	5.00×10^{-1}	1
$\frac{1}{2}S_8 + e^- \rightleftharpoons \frac{1}{2}S_8^{-2}$	2.471	1.90	1
$\frac{3}{2}S_8^{-2} + e^- \rightleftharpoons 2S_6^{-2}$	2.433	2.00×10^{-2}	1
$S_6^{-2} + e^- \rightleftharpoons \frac{3}{2}S_4^{-2}$	2.444	2.00×10^{-2}	1
$\frac{1}{2}S_4^{-2} + e^- \rightleftharpoons S_2^{-2}$	2.447	2.00×10^{-4}	1
$\frac{1}{2}S_2^{-2} + e^- \rightleftharpoons S^{-2}$	2.458	2.00×10^{-7}	1

Table S7. Mechanical parameters of various components.

Components	Young's modulus (GPa)	Poisson's ratio	Density (kg m^{-3})

Separator	1.00	0.25	1.01×10^3
Li metal	2.00	0.34	5.34×10^2
Cathode	5.00	0.25	2.36×10^3
S_8 molecules	-	-	2.07×10^3
Li_2S molecules	-	-	1.92×10^3

Table S8. Comparison of capacity performance in low-temperature of our Li-S cell based on the S/IGCL-NFE with other reported work[5-8].

Samples	**Cycled Capacity (mAh g^{-1})**	**Capacity Retention (%)**	**Cycle number**	**E/S**	**S loading (mg cm^{-2})**	**Ref.**
$BiVO_4$	700.0	87.5	100	8.0	2.0	6
ZnS@HPCS	750.0	75.0	90	18.0	1.5	7
HCEs	340.0	83.0	100	10.0	2.0	8
LCEs	400.0	80.0	100	10.0	2.3	9
S/IGCL-NFE	1313.9	113.2	100	5.0	4.1	This work

Table S9. Component details of the Li-S pouch cell with an S loading of 300.0 mg.

Pouch cell overview	
Cathode (single)	4.68 mg cm^{-2}
Electrolyte	3.00 μL mg^{-1}
Cu foil	4.48 mg cm^{-2}
Al foil	2.16 mg cm^{-2}
Anode (single)	2.67 mg cm^{-2}
Separator	0.81 mg cm^{-2}
Cu foil thickness	5.0 μm
Al foil thickness	8.0 μm
Separator thickness	15.0 μm
Number of cathode layers	2
Number of Anode layers	3
Number of separator layers	4
Tap&package	1.01 g
N/P	1.27
Energy density (without Tap&package)	400.2 Wh kg^{-1}

Table S10. Component details of the Li-S pouch cell based on the dry electrode (S loading:18.70 mg cm^{-2}).

Pouch cell overview	
Cathode (single)	18.70 mg cm^{-2}
Electrolyte	3.00 μL mg^{-1}
Cu foil	4.48 mg cm^{-2}
Al foil	2.16 mg cm^{-2}
Anode (single)	10.68 mg cm^{-2}
Separator	0.81 mg cm^{-2}
Cu foil thickness	5.0 μm
Al foil thickness	8.0 μm
Separator thickness	15.0 μm
Number of cathode layers	1
Number of Anode layers	1
Number of separator layers	1
Tap&package	1.01 g
N/P	1.27
Energy density (without Tap&package)	430.6 Wh kg^{-1}

Table S11. Electrochemical performance under high sulfur loading comparison of our work with previous work[9-16].

Samples	S loading (mg cm^{-2})	Areal capacity (mAh cm^{-2})	E/S	Ref.
$\{Co_4W_{18}\}$/rGO	5.6	4.5	4.5	10
Fe-Co DACs	8.6	9.5	8.2	11
CoNi MOF	4.6	4.2	20.0	12
S@N-$MoSe_{2-x}$/C	6.2	7.3	6.3	13
SP-Fe_3O_4-C	8.2	6.5	6.0	14
S/C/CMC	13.0	15.0	7.6	15
S@V-S_1N_3	4.2	4.1	10.0	16
Mo_2C	6.0	6.3	4.9	17
S/IGCL-NFE	18.7	19.5	3.0	This work

REFERENCES

1. B. Wang, L. Wang, M. Mamoor, C. Wang, Y. Zhai, F. Wang, Z. Jing, G. Qu, Y. Kong and L. Xu, *Angew. Chem., Int. Ed.*, 2024, **63**, e202406065.
2. J. T. Kim, H. Su, Y. Zhong, C. Wang, H. Wu, D. Zhao, C. Wang, X. Sun and Y. Li, *Nat. Chem. Eng.*, 2024, **1**, 400-410.
3. L. Nie, R. Gao, M. Zhang, Y. Zhu, X. Wu, Z. Lao and G. Zhou, *Adv. Energy Mater.*, 2024, **14**, 2302476.
4. Y. Luo, S. Pan, J. Tian, Y. Liang, H. Zhong, R. Ma, J. Gu, Y. Wu, H. Zhang, H. Lin, W. Huang, Y. Deng, Y. Su, Z. Gong, J. Huang, Z. Hu and Y. Yang, *Adv. Mater.*, 2024, **36**, 2413325.
5. L. Hu, T. Yang, X. Yan, Y. Liu, W. Zhang, J. Zhang, Y. Xia, Y. Wang, Y. Gan, X. He, X. Xia, R. Fang, X. Tao and H. Huang, *ACS Nano*, 2024, **18**, 8463-8474.
6. D.-R. Deng, H.-J. Xiong, Y.-L. Luo, K.-M. Yu, J.-C. Weng, G.-F. Li, J. Lei, Y. Li, M.-S. Zheng and Q.-H. Wu, *Adv. Mater.*, 2024, **36**, 2406135.
7. H. Ding, Z. Chen, H. Li, H. Suo, C. Liu, H. Yu, J. Yuan, Z. Sun, Y. Zhu and B. Song, *Nano Lett.*, 2024, **24**, 15118-15126.
8. D. Guo, S. Thomas, J. K. El-Demellawi, Z. Shi, Z. Zhao, C. G. Canlas, Y. Lei, J. Yin, Y. Zhang, M. N. Hedhili, M. Arsalan, Y. Zhu, O. M. Bakr, O. F. Mohammed and H. N. Alshareef, *Energy Environ. Sci.*, 2024, **17**, 8151-8161.
9. Z. Guan, X. Chen, F. Chu, R. Deng, S. Wang, J. Liu and F. Wu, *Adv. Energy Mater.*, 2023, **13**, 2302850.
10. J. Lei, X.-X. Fan, T. Liu, P. Xu, Q. Hou, K. Li, R.-M. Yuan, M.-S. Zheng, Q.-F. Dong and J.-J. Chen, *Nat. Commun.*, 2022, **13**, 202.
11. X. Sun, Y. Qiu, B. Jiang, Z. Chen, C. Zhao, H. Zhou, L. Yang, L. Fan, Y. Zhang and N. Zhang, *Nat. Commun.*, 2023, **14**, 291.
12. X. Ren, Q. Wang, Y. Pu, Q. Sun, W. Sun and L. Lu, *Adv. Mater.*, 2023, **35**, 2304120.
13. Z. Shi, Z. Sun, J. Cai, X. Yang, C. Wei, M. Wang, Y. Ding and J. Sun, *Adv. Mater.*, 2021, **33**, 2103050.
14. H. Zhang, M. Zhang, R. Liu, T. He, L. Xiang, X. Wu, Z. Piao, Y. Jia, C. Zhang, H. Li, F. Xu, G. Zhou and Y. Mai, *Nat. Commun.*, 2024, **15**, 5451.
15. M. Shaibani, M. S. Mirshekarloo, R. Singh, C. D. Easton, M. C. D. Cooray, N. Eshraghi, T. Abendroth, S. Dörfler, H. Althues, S. Kaskel, A. F. Hollenkamp, M. R. Hill and M. Majumder, *Sci. Adv.*, 2020, **6**, eaay2757.
16. R. Yan, Z. Zhao, R. Zhu, M. Wu, X. Liu, M. Adeli, B. Yin, C. Cheng and S. Li, *Angew. Chem., Int. Ed.*, 2024, **63**, e202404019.
17. K. Um, C. Jung, H. Nam, H. Lee, S. Yeom and J. H. Moon, *Energy Environ. Sci.*, 2024, **17**, 9112-9121.